magnetochemistry

Review

Principles of Magnetic Hyperthermia: A Focus on Using Multifunctional Hybrid Magnetic Nanoparticles

Ihab M. Obaidat [1,*], Venkatesha Narayanaswamy [2], Sulaiman Alaabed [2], Sangaraju Sambasivam [1] and Chandu V. V. Muralee Gopi [3]

[1] Department of Physics, United Arab Emirates University, Al-Ain 15551, UAE; sambaphy@gmail.com
[2] Department of Geology, United Arab Emirates University, Al-Ain 15551, UAE; venkateshnrn@gmail.com (V.N.); s.alaabed@uaeu.ac.ae (S.A.)
[3] School of Electrical and Computer Engineering, Pusan National University, Busan 46241, Korea; naga5673@gmail.com
* Correspondence: iobaidat@uaeu.ac.ae; Tel.: +971(3)-7136321; Fax: +971(3)-7136944

Received: 11 October 2019; Accepted: 29 November 2019; Published: 6 December 2019

Abstract: Hyperthermia is a noninvasive method that uses heat for cancer therapy where high temperatures have a damaging effect on tumor cells. However, large amounts of heat need to be delivered, which could have negative effects on healthy tissues. Thus, to minimize the negative side effects on healthy cells, a large amount of heat must be delivered only to the tumor cells. Magnetic hyperthermia (MH) uses magnetic nanoparticles particles (MNPs) that are exposed to alternating magnetic field (AMF) to generate heat in local regions (tissues or cells). This cancer therapy method has several advantages, such as (a) it is noninvasive, thus requiring surgery, and (b) it is local, and thus does not damage health cells. However, there are several issues that need to achieved: (a) the MNPs should be biocompatible, biodegradable, with good colloidal stability (b) the MNPs should be successfully delivered to the tumor cells, (c) the MNPs should be used with small amounts and thus MNPs with large heat generation capabilities are required, (d) the AMF used to heat the MNPs should meet safety conditions with limited frequency and amplitude ranges, (e) the changes of temperature should be traced at the cellular level with accurate and noninvasive techniques, (f) factors affecting heat transport from the MNPs to the cells must be understood, and (g) the effect of temperature on the biological mechanisms of cells should be clearly understood. Thus, in this multidisciplinary field, research is needed to investigate these issues. In this report, we shed some light on the principles of heat generation by MNPs in AMF, the limitations and challenges of MH, and the applications of MH using multifunctional hybrid MNPs.

Keywords: magnetic hyperthermia; cancer; nanoparticles; magnetic relaxation; magnetic anisotropy; heat generation; multifunctional nanoparticles; graphene oxide; photothermal therapy

1. Introduction

1.1. Effects and Categories of Hyperthermia

Hyperthermia which is the treating of diseases by heating was known since the ancient era [1]. Increasing the temperature of cells above 41 °C is known to cause some effects in the membrane and interior of the cell, such as (a) increasing the fluidity and permeability of the cell membrane, (b) slowing down of the mechanisms of synthesis of nucleic acid and protein, (c) inducing protein denaturation and agglomeration, and (d) damaging the tumor vasculature resulting in a decrease of blood flow [2].

Hyperthermia is divided into three main categories depending on the size of the cancer region being treated [3–5]: whole-body, regional, and local hyperthermia. In the whole-body hyperthermia approach, heat is applied to the whole body in several ways such as using hot water blankets, electric blankets and hot wax. In the regional hyperthermia method, heat is applied to a whole organ or region of the body using external arrays of applicators, and regional perfusion. In local hyperthermia, heat is applied to small tumor regions using electromagnetic waves such as radio waves, microwaves, and ultrasound, which are generated by applicators that are placed at the surface or under skin of superficial cancer or implanted inside the targeted region. In these methods, the temperature must be increased between 41 °C and 45 °C. Each one of these has its negatives. Some of these negatives [2,6] are in all these techniques: (a) heat is applied to the healthy cells in addition to the unhealthy ones which could cause negative side effects, (b) temperature control and measurement at the cell level is difficult, (c) the applied heat is not uniform through the targeted region, and (d) the amount of heat delivered is small. In local hyperthermia, there is a better control on the area exposed to heat and a better heat uniformity. However, local hyperthermia sufferers from two main drawbacks: (a) it is highly invasive for deep cancer regions and (b) the small penetration depth, which is approximately a few centimeters. These drawbacks of local hyperthermia make it better used for small and superficial cancer regions. Nanotechnology can help in eliminating these two negatives of local hyperthermia. Using local hyperthermia with magnetic nanoparticles (MNPs) that are delivered only to the cancer cells and heated externally by an alternating magnetic field (AMF) makes it a noninvasive method, minimizes the side effects and allows for targeting deep cancer cells [5].

Note that for practical applications of MH, the MNPs should have narrow size distribution. Particles with considerably different sizes will result in inhomogeneous heat generation in tissues. This means that while the heat generated through the whole tissue is still below the required value, some parts in the tissue might get overheated causing negative side effects. Also, note that for in vivo hyperthermia experiments, it is difficult to measure the temperature of deep parts of the targeted body. In addition, measuring the temperature at the cell level is not yet permitted. For in vivo experiments, the MNPs can be injected directly in the tumor region or through blood (intravenous administration). In the latter case, two main issues should be resolved; (a) the MNP concentration should be large enough to generate the required amount of heat, and (b) the size of the MNPs to be used should be between 5 nm and 100 nm. If the size of MNPs is less than 5 nm, they will be eliminated through the kidney, whereas particles larger than 100 nm will be cleared by macrophages and moved to the liver [7]. The blood circulation time will thus be minimized and thus the chances for particles to reach the targeted region with enough concentration will be reduced. Additionally, note that Brownian relaxation (will be discussed later) is prevented or minimized in vitro and in vivo experiments when the MNPs are placed in cells or on their membranes. Thus, Neel relaxation will dominate. Thus, hyperthermia measurements are important not only in aqueous suspension, but also in media that is similar to the targeted tissue [8]. In addition, for in vivo experiments, reasonable data is obtained only when the frequency and amplitude of the AMF satisfy the safety criteria.

Several review papers and books discussed the physics and application of MH using MNPs [9–21]. In this report, we present the principles of MH and the physics of heat generation. We also discuss how to measure the power dissipation using calorimetry methods. We also discuss the multifunctional applications of MNPs.

1.2. Magnetic Nanoparticles for Local Hyperthermia

The magnetic properties of MNPs are determined by two main features: (a) finite-size effects and (b) surface effects [16]. Finite-size effects are related to the structure of the NP (single-domain or multidomain). On the other hand, surface effects result from several effects such as the symmetry breaking of the crystal structure at the surface of the particle, dangling bonds, oxidation, and surface stain. The role of surface effects increases as the particle size decreases. This is the case because the ratio of the number of surface atoms to the core atoms increases as the particle size decreases. Due to size-effects and surface effects, magnetic properties of MNPs, such as magnetic moment per atom, saturation magnetization, magnetic anisotropy, coercivity, and Curie temperature, can differ from those of a bulk material [16,22]. The preferred size of the MNPs in most medical applications, is between 10 and 50 nm. Usually, MNPs become single domain particles and display superparamagnetic behavior above a certain temperature called the blocking temperature. In the superparamagnetic state, a nanoparticle has a large magnetic moment and behaves like a giant paramagnetic atom with a fast response to applied magnetic fields with almost zero magnetic reminiscence and coercivity. For MH applications, MNPs must possess large saturation magnetization: M_s values that will generate large amount of heat in the tumor cells under the application of AMF. In addition, large M_s values allow for more control on the movement of the MNPs in the blood using external magnetic field [23]. In addition to the requirement of large M_s, MNPs should be superparamagnetic to achieve good colloidal stability. In the absence of an applied magnetic field, the MNPs in superparamagnetic state lose their magnetism at temperatures above the blocking temperature. This guarantees that the particles will not aggregate and thus they will maintain their colloidal stability. In addition, the interparticle (dipolar) interactions between MNPs decrease with the decrease of the size of particles. This can be understood since the dipole–dipole interaction energy scales as r^6 (r is the interparticle distance). Thus, the small dipolar interactions will result in minimizing the particle aggregation in the existence of applied magnetic field. However, it is important to understand that these two conditions on MNPs (with large M_s and superparamagnetic) should not be isolated from other factors that affect heat generation. For example, heating power was found to be maximized in large ferromagnetic NPs with low anisotropy [23]. Also, the optimum size for the maximum power loss was found to vary with the amplitude of the applied magnetic field [24] and frequency as well. Therefore, several experimental conditions should be considered before we can decide on the choice between superparamagnetic and larger ferromagnetic NPs for MH.

Iron oxide nanoparticles (IONPs), such as magnetite (Fe_3O_4) and maghemite (γ-Fe_2O_3), have good magnetic properties [25,26] that can be tuned by (a) changing synthesis methods, (b) changing the shape and size, (c) modifying the surface structure, (d) and synthesizing core–shell structures with tunable interface exchange anisotropy. The IONPs are good candidates for hyperthermia applications [25,27] due to (a) the ease of synthesis with small sizes and well controlled size distribution, (b) their biocompatibility, and (c) their biodegradability. Although the IONPs are degraded in human body, iron atoms are released. The metabolic mechanisms in humans can manage the released iron atoms by storing or transferring them [28,29].

2. Heat Generation

2.1. Magnetic Relaxation Processes

Magnetocrystalline (or magnetic) anisotropy in magnetic materials results from the spin-orbital interactions of the electrons. The magnetic anisotropy is responsible for keeping the magnetic moments in a particular direction. Atomic orbitals mainly have nonspherical shapes, and thus they tend to align in a specific crystallographic direction. This preferred direction is called the easy direction. In magnetic materials with large magnetic anisotropy the atomic spin and the orbital angular moments are strongly coupled and thus the magnetization prefers to align along the easy direction. Energy (called the anisotropy energy) is needed to rotate the magnetization away from the easy direction. For uniaxial anisotropy, the anisotropy energy per particle is given by [30]

$$E = K\ V\ sin^2\theta + higher\ order\ terms \tag{1}$$

Here, K is the anisotropy constant (it includes all sources of anisotropy and has a unit of J/m^3), V is the magnetic volume of the particle, and θ is the angle between the particle magnetization and the easy magnetization axis. The higher order terms are very small compared with the first term, and thus can be ignored. In this case, there is only one easy axis with two energy minima separated by the energy maximum, KV.

From Equation (1), we can see that the anisotropy energy is directly proportional to the particle size and to the anisotropy constant. For a fixed K, when the particle size, V decreases the anisotropy energy, E decreases. When V gets very small (reaching the single magnetic domain region), E (which holds the magnetic moment of the particle along the easy axis) might become smaller than the thermal energy, $E_{\mathrm{th}} = k_{\mathrm{B}}T$ (k_{B} is the Boltzmann constant). The particle magnetic moment thus starts to flip freely and randomly in all directions leading to zero net magnetization (in the absence of an external magnetic field). When a magnetic field is applied, energy is given to the particles which will force the magnetic moments of the particles to align along the field direction away from the easy axis. When the field is removed (as with AMF), the magnetic moments will return back (relax) and align along the easy axis. Thus, the gained energy by the applied magnetic field will be lost as heat. If the applied field is AMF, this aligning and relaxation of moments processes will continue, and thus heat will be generated as long as the AMF is applied.

When the orientation of the particle itself is not allowed to change (no physical rotation) during the flipping of its magnetic moment, then the relaxation time of the moment of the particle is called the Néel relaxation time, τ_{N} and is given by [15,31–33]

$$\tau_{\mathrm{N}} = \frac{\tau_o}{2}\sqrt{\frac{\pi k_{\mathrm{B}}T}{K_{\mathrm{eff}}V}}\exp\left(\frac{K_{\mathrm{eff}}V}{k_{\mathrm{B}}T}\right) \tag{2}$$

where K_{eff} is the effective magnetic anisotropy and the factor $\tau_0 \approx 10^{-13}$–$10^{-9}s$ [10,34].

In a magnetic measurement, we call τ_{m} the measurement time. When the magnetization of a MNP is measured, where $\tau_{\mathrm{m}} \gg \tau_{\mathrm{N}}$, the magnetic moment of the MNP will flip several times (randomly) during the measurement giving zero average magnetization. In this case, the MNP is said to be in the superparamagnetic state. On the other hand, when $\tau_{\mathrm{m}} \ll \tau_{\mathrm{N}}$ the magnetic moment of the particle will not have enough time to flip during the measurement and thus the moment will be blocked at the initial non-zero value at the beginning of the measurement. In this case, the NP is said to be in the blocked state. When $\tau_{\mathrm{m}} = \tau_{\mathrm{N}}$, a transition between the superparamagnetic state and the blocked state occurs [30]. Therefore, at T_{b}, the Néel relaxation time will be equal to the measurement time, $\tau_{\mathrm{N}} = \tau_{\mathrm{m}}$. In the superparamagnetic state, no magnetization appears when applied magnetic field is zero.

In magnetization experiments the measurement time is usually kept constant while the temperature is varied. In such case the transition between superparamagnetic and blocked states is obtained as a function of temperature. The temperature at which this transition occurs is called the blocking temperature, T_{b}. In addition to its dependence on the particle size and magnetic anisotropy, the blocking temperature also depends on other factors such as particle-particle interactions. When the MNPs are exposed to a magnetic field, their magnetic moments will be forced to align along the magnetic field direction. If the particles can (physically) rotate and their magnetic anisotropy is large enough, the magnetic field might be successful in causing the particles to physically rotate by pinning their moments. Once the field is removed, the particles will start rotating again and the magnetic moments will relax. This relaxation of magnetic moments is called the Brownian relaxation mechanism, τ_{B} and is given by [15,31,35]

$$\tau_{\mathrm{B}} = \frac{3\,V_{\mathrm{H}}\,\eta}{k_{\mathrm{B}}\,T} \tag{3}$$

where η is the viscosity of the liquid containing the particles and V_{H} is the hydrodynamic volume of the particle. The hydrodynamic volume includes the magnetic volume and the attached layers on the surface. These attached layers are due to particle coating, absorbed surfactants or interaction with the fluid. Therefore, V_{H} is larger than the original volume of the particle, V. The physical rotation of the MNPs will cause friction between the particles and the medium in which they exist and heat will be generated. This generated heat will depend on the hydrodynamic volume and the viscosity of the medium.

If both moments relaxation processes exist, the effective magnetic relaxation time, τ_{eff} is then given by

$$\frac{1}{\tau_{\mathrm{eff}}} = \frac{1}{\tau_{\mathrm{N}}} + \frac{1}{\tau_{\mathrm{B}}} \tag{4}$$

As evident from Equation (4), the effective relaxation time, τ_{eff}, is determined by the shorter relaxation time (τ_{N} or τ_{B}). For large particles in low viscosity medium, Brownian relaxation mechanism dominates while for small particles in high viscous medium Néel relaxation mechanism dominates. For MNPs with an average size smaller than 15 nm, τ_{N} is smaller than τ_{B}, and therefore τ_{eff} is dominated by τ_{N}, whereas for MNPs with average size larger than 15 nm, τ_{B} is smaller than τ_{N}, and therefore τ_{eff} is dominated by τ_{B} [31]. In in vivo MH experiments, both of these mechanisms are expected to contribute in generating heat. It is important to realize that Equations (3) and (4) were derived for single-domain and identical particles (same size and shape) that are isolated from each other (non-interacting particles). In addition, Equations (1) and (2) are valid for zero (or very small) applied magnetic field. If the applied field is not zero, then Zeeman energy should be included [15].

2.2. Power Loss in MNPs in AMF

For efficient in vivo hyperthermia experiment, we need to generate large SAR values while maintaining safety conditions. Safety conditions include (a) the use of minimum amounts of MNPs and (b) the use of an AMF that will not cause negative side effects due to the induced eddy currents in living tissues. To satisfy the first condition, we need to produce MNPs with optimal magnetic properties that will lead to large heat generation at low concentrations. These properties include saturation magnetization and effective magnetic anisotropy. These properties depend on the size, size distribution, interparticle interactions, particle composition, particle shape, and structure such as MNPs with single magnetic core or MNPs with magnetic core and magnetic shell (called bimagnetic core–shell particles). To satisfy the second condition an AMF with will defined range of intensity and frequency is needed.

In an adiabatic process, the internal energy of a magnetic system is equal to the magnetic work done on it [35]:

$$U = -\mu_0 \oint M\mathrm{d}H \tag{5}$$

During a complete magnetic field cycle, the power dissipation in the magnetic system is equal to the internal energy divided by the time field cycle. Thus, during several field cycles the power dissipation, is equal to internal energy multiplied by the frequency:

$$P = Uf \tag{6}$$

The power dissipated in superparamagnetic NPs, due to the application of an AMF of maximum strength H_o and frequency f ($\omega = 2\pi f$), was suggested to depend on magnetic moment relaxations and is given by [35]

$$P(f,\, H) = Uf = \pi\mu_0\chi'' {H_o}^2 f \tag{7}$$

where μ_0 is the permeability of free space and χ'' is the imaginary part of the susceptibility χ ($\chi = \chi' - i\chi''$). In the linear response theory (LRT) the magnetization, M is assumed to have linear relation with the applied magnetic field, H, and thus χ remains constant with increasing H ($M = \chi H$). The LRT can be applied for very small magnetic fields. Therefore, it can be stated that the LRT is valid in the superparamagnetic regime where $H_{\mathrm{max}} < k_{\mathrm{B}}T/\mu_0 M_{\mathrm{s}} V$ and when the magnetization of MNPs is linearly proportional to the applied magnetic field. Therefore, in the LRT the magnetic fields should be much smaller than the saturation field (the field required to produce saturation magnetization) of the MNPs ($H_{\mathrm{max}} \ll H_{\mathrm{K}}$). Here, H_{max} is the amplitude of the AMF and H_{K} is the anisotropy field [23].

Thus, when the LRT is assumed, the real part (in-phase component) of the magnetic susceptibility, χ' is given by

$$\chi' = \chi_0 \frac{1}{1 + \left(2\pi f \tau_{eff}\right)^2} \tag{8}$$

The imaginary part (out-of-phase component) of the susceptibility, χ'' is given by [36,37]

$$\chi'' = \chi_0 \frac{2\pi f \tau_{eff}}{1 + \left(2\pi f \tau_{eff}\right)^2} \tag{9}$$

The initial constant susceptibility χ_0 is given by

$$\chi_0 = \frac{\mu_0 M_s^2 V}{k_B T} \tag{10}$$

The heating efficiency is represented by the specific absorption rate (SAR) which is also referred to as the specific loss power (SLP). SAR is measured in watts per gram and is given by [38]

$$\mathrm{SAR}(f, H) = \frac{P(f,\ H)}{\rho} = \frac{\pi \mu_0 \chi'' H^2 f}{\rho} \tag{11}$$

where ρ is the mass density of the magnetic material.

In order for the MNPs to have a practical safe application in MH the MNPs should produce large SAR values. This is needed because of two reasons: (a) for safety measures, the MNPs should be used in small concentrations, and (b) in living organs, the water-based medium around the cells absorb a lot of the heat generated by the MNPs. In Rosensweig's theory or LRT, the heat generation of the MNPs depends on several factors such as: strength and frequency of the applied magnetic field, the solvent viscosity, the size of the particles, the saturation magnetization and the magnetic anisotropy of the MNPs. For safety requirements, the strength and frequency of the AMF cannot have any value for applications on living organs. This is because eddy currents are induced in a conductor due to an AMF and thus produce heating in the conductor. As water is a conductor, in human body eddy currents can be induced under an AMF which could result in damaging effect. In general, the parameters that determine the heat generation in MH using MNPs can be classified into two categories: intrinsic and extrinsic parameters. Intrinsic parameters are related to properties of the single isolated MNP. Magnetic anisotropy, size, composition, structure, magnetization, and shape are examples of intrinsic parameters. On the other hand, extrinsic parameters are related to effects that have to do with environment of the MNPs such as the parameters of the AMF (frequency, strength, homogeneity, …), the distance between the MNPs (concentration or agglomeration), the viscosity of the medium, and electric conducting properties of the tissues. In the following sections, we will focus on one intrinsic parameter which is the anisotropy and on two extrinsic parameters which are the agglomeration parameter and the AMF parameters (frequency and amplitude).

3. Intrinsic Parameters

3.1. Overview of Intrinsic Parameters

Intrinsic parameters include, structure, composition, phase (crystalline or amorphous), shape, size distribution, magnetization, and magnetic anisotropy. Several actions can affect the intrinsic parameters of MNPs such as doping [39–41], surface and interface effects [26,42]. Under an AMF, heat generation by MNPs is determined by hysteresis loss and relaxation effects [43]. Magnetic hysteresis loss occurs in large MNPs with more than one magnetic domain. Domain wall motion due to the applied magnetic field will cause heat loss [44]. These large MNPs will always display magnetic hysteresis regardless if the applied magnetic field is constant (DC) or is AMF. In small MNPs with single magnetic domain (these are called superparamagnetic nanoparticles), heat loss is caused by magnetic relaxation processes. In these small MNPs no magnetic hysteresis is displayed in DC applied magnetic field. However, when these MNPs are placed in an AMF magnetic hysteresis will be displayed due to Brownian and Neel relaxation processes.

In addition to the MNPs volume and the viscosity of the medium in which they exist, Brownian and Neel relaxation processes are determined also by the magnetocrystalline anisotropy of the material. This type of anisotropy determines along which direction the magnetic moments of the material tend to align. However, SAR values depend not only on the magnetocrystalline anisotropy, but on the effective anisotropy which is the net magnetic anisotropy of the MNP.

3.2. The Effective Magnetic Anisotropy

To minimize the negative side effects, the dosage of MNPs required for MH treatment should be reduced. Thus, it becomes necessary to use MNPs with the best heating capability. Magnetic anisotropy is an important intrinsic parameter of MNPs that can be tuned to vary the heating efficiency. However, tuning the magnetic anisotropy of MNPs is a challenging task. The effective anisotropy has four main components: (a) the magnetocrystalline anisotropy, (b) shape anisotropy, (c) surface anisotropy, and (d) exchange anisotropy at the interface of core–shell MNPs. All these types can be tuned. The magnetocrystalline anisotropy can be modified by doping the iron oxides with other elements [41]. The shape anisotropy can be changed by changing the shape of the MNPs from spherical to cubic or other shapes [45–47]. Surface anisotropy which results from surface spin effects can be modified by coating the MNPs [48].

The magnetic anisotropy of MNPs can be varied by synthesizing particles with bimagnetic core–shell phases [49,50]. Theses bimagnetic core–shell MNPs with two different magnetic phases exhibit very interesting properties [51,52]. The magnetic properties (including magnetic anisotropy) of the bimagnetic core–shell MNPs can be tailored by manipulating the interfacial exchange interaction between the core and shell phases [48,53]. This can be achieved by several ways: (a) selecting of the many possible combinations of the core–shell phases, (b) controlling core and shell dimensions [54], and (c) by controlling the interface quality [55–57]. Exchange coupling at the core–shell interface of the MNPs could result in extremely large SAR values [41]. Large number of reports discussed the exchange bias in MNPs with bimagnetic core–shell structures [58–60]. However, the origin of the exchange bias is not fully understood. One of the interesting models reported to describe the exchange bias in bimagnetic materials is based on the existence of interfacial spin-glass-like structures. The interfacial spin-glass-like structures prevent the direct exchange coupling of the core and shell moments.

Low symmetry near the surface causes large contribution to the local magnetic anisotropy, resulting in spin canting [61]. Lattice mismatching between the shell and core materials in the core–shell MNPs could result in large degree of interfacial structural disorder. The smaller the core diameter, the larger is the interfacial structural disorder [62]. This is suggested to case also at the core–shell interface where interfacial canted spins can freeze into spin-glass-structures. Randomly spread spin-glass-like phases at the interfaces of bimagnetic layered and core–shell interfaces were suggested to significantly influence the exchange bias effect [58,63,64].

4. Extrinsic Parameters

4.1. Parameters of the AMF

In all types of experimental methods (which will be discussed in the next section), a source of AMF is needed to heat the MNPs. Heat will be conducted to targeted cells through the living tissues. This displays the necessity to understand such heat conduction and to accurately monitor the changes in the target temperature. The AMF is usually generated using a solenoid [65] or Helmholtz coil [66]. The coil diameter is determined by the sample size. The sample is insulated from the coil by vacuum or a material that has low thermal conductivity and is placed at the center of the coil where the field is most homogeneous. The well-controlled cooling process of the coil is an important task to maintain during the experiment. If the coil becomes very hot, indirect heating of the sample by the heat irradiated from the hot coil itself will occur. On the other hand, if the coil is cold, the sample might get cooled by the coil [67]. If one of these processes occurs, the SAR data will not be reliable. For effective cooling, the coils are usually made of copper tubes to allow cooling water to go through the wire.

As discussed in the previous section, the SAR values depend on the frequency, f, and amplitude, H_o, of the AMF. In theory, large amount of heat can be generated by increasing these two parameters. However, practically this is not possible due to two main reasons: (a) difficulties in designing equipment needed to generate large frequency and high field and (b) increased harm to healthy cells due to induced eddy currents at high f and H_o. The frequency of AMF that will cause reasonable heating in MH is limited within the range of 50 kHz $< f <$ 1 MHz. Above 1 MHz, negative physiological reposes might occur [21]. On the other hand, the field amplitude is limited to H_o < 15 kA/m, which is based on estimation of the heat dissipation by the induced eddy current [21]. Several safety conditions in terms of the product $H_o f$ were suggested [68]. One of these safety conditions is called Atkinson–Brezovich limit of $H_o f < 4.85 \times 10^8$ $\mathrm{Am^{-1}s^{-1}}$ (6×10^6 Oe Hz) [69], which was suggested based on real tests on patients who were exposed to AMF for a duration that exceeds 1 h. The value of the product $H_o f$ at which the patents started feeling considerable discomfort was found to be 4.85×10^8 $\mathrm{Am^{-1}s^{-1}}$. Another safety condition was suggested to be $H_o f < 5 \times 10^9$ $\mathrm{Am^{-1}s^{-1}}$ (6.25×10^7 Oe Hz) [69]. This limit is 10 times greater than the Atkinson–Brezovich limit and was suggested to be applied to small regions of the body of patients whose lives might be in jeopardy. A third safety condition was suggested to be $H_o f < 2 \times 10^8$ $\mathrm{Am^{-1}s^{-1}}$ [70]. This limit is based on a simulation study of the heat resulted from the electromagnetic field distribution in a model of human body. As can be realized that none of these limits is based on real measurements of the effect of the AMF parameters on the functions of cells, and thus further research is needed. Based on Atkinson–Brezovich limit, if the frequency of the AMF is fixed at 100 kHz (which is very suitable for medical applications), H_o must have values be between 4.85×10^3 $\mathrm{Am^{-1}}$ (60 Oe) and 50×10^3 $\mathrm{Am^{-1}}$ (625 Oe) [71].

4.2. Role of Interparticle Interactions on the Heating Efficiency

The dipolar interaction is a long range interaction where the interaction energy is proportional to $1/r^6$, where r is the interparticle distance. Therefore, dipolar interactions between MNPs decrease strongly with increasing the interparticle distance. This means that particles with small concentrations will experience small dipolar interactions. Strong dipolar interactions are expected to have an impact on the magnetic relaxations of MNPs, and thus on their heating efficiency in the existence of an AMF. In clinical treatments using MH, the concentrations of MNPs is 112 mg Fe/mL, while in MH experiments the concentrations used are much smaller, usually between 0.1 and 30 mg/mL [72–83]. The high concentration of MNPs in clinical treatments result in smaller interparticle distances and thus large dipolar interactions that could lead to agglomerations or aggregates. The agglomerations could have a negative influence on the heating efficiency of the MNPs due to hindered relaxation processes [31,73]. Although several theoretical and experimental studies were conducted to reveal the role of dipolar interactions on heating efficiency in MH, there is no complete understanding of this topic yet due to contradiction results that could have several sources [24,84–86]. By calculating $\omega\tau$ in some conflicting reports [31], the authors suggested that MNP concentration always suppresses the relaxation time. However, this reduction in relaxation time could have opposite effects on SAR depending on whether the value of $\omega\tau > 1$ or $\omega\tau < 1$. They suggested that when $\omega\tau < 1$, SAR decreases as the relaxation time and τ decreases, whereas for $\omega\tau > 1$, SAR increases as τ decreases.

4.3. Beyond the LRT

LRT is only applicable at very small applied magnetic fields. Therefore, for MNPs with low anisotropy energies the LRT will not be applicable where the magnetization saturation is reached at small magnetic fields. In such case, the Stoner–Wohlfarth model is an option. The standard Stoner–Wohlfarth model is applicable when $T = 0$ (or in the limit of infinite frequency). If the magnetization of the MNPs needs to flip direction between the two equilibrium positions (potential wells) it must overcome the energy barrier between the potential wells. Since $T = 0$, thermal energy cannot provide such energy. Thus, the applied magnetic field will provide the needed energy. Researchers investigated a modification to Stoner–Wohlfarth model where thermal activation of magnetization and the sweeping rate of the AMF were included [23]. The role of frequency and finite temperature on the areas of hysteresis loops and coercivity were studied where analytical formulas for such dependence were obtained. In other studies, the dynamics of rotatable MNPs in aqueous phase (which resembles the cytoplasm) were studied in a large AMF using numerical simulations [87,88].

Monodisperse spheroidal MNPs with non-magnetic surfactant layers were considered. The MNPs were considered to be uniformly dispersed with no aggregation due to the absence of dipolar interactions. A two-level approximation was used where thermal activation causes reversals between two meta-stable directions. The outcomes of the study could not be explained by the conventional models that consider a linear response of thermodynamic equilibrium states ($H_0 = 0,\ T \neq 0$) or the Stoner–Wohlfarth model of magnetic field-driven reversals ($H_0 \neq 0,\ T = 0$).

In MH experiments, the MNPs are dispersed in a liquid medium. The application of an AMF will result in complex dynamics of MNPs in such viscous liquid. These complex dynamics are ignored in the conventional LRT causing oversimplification of the real situation. Stochastic equations of motion were used to study the dynamics of an assembly of MNPs dispersed in a viscous Liquid [89]. It was found that SAR values of an assembly of MNPs in a liquid can be considerably enhanced by selecting a suitable mode of magnetization oscillations. For H_0 = 200–300 Oe and f = 300–500 kHz, with magnetic parameters typical for iron oxides, the SAR values can be of the order of 1 kW/g. This result clearly displays the significant difference between the magnetic dynamics of MNPs dispersed in a viscous liquid from that of immobilized MNPs in a solid matrix.

Uniaxial superparamagnetic particles suspended in a viscous fluid and subjected to an AMF were studied [90]. Néel and Brownian magnetic relaxations were considered. Significant contribution to the full magnetic response of the particles (and thus to the specific loss power) was obtained due to the viscous losses because of the particle motion in the fluid; a modification to the conventional LRT, where the field-dependent Brownian relaxation time is suggested to replace the field-independent one.

In [23], the authors reported three types of theories can be used to describe hysteresis loops of MNPs: the LRT, equilibrium functions, and theories based on Stoner–Wohlfarth model. Limitations and domains of validity of each theory were discussed. The authors proposed that the separation between "hysteresis losses" and "relaxation losses" is artificial and not correct. The LRT was shown to be pertinent only for MNPs with strong anisotropy. Theories based on Stoner–Wohlfarth model should be used for particles with small anisotropy. On the other hand, the LRT including Brownian motion was suggested to be valid only for small magnetic fields [23,91].

5. Experimental and Theoretical Limitations in the Determination of SAR

There are two main experimental approaches that can be used to measure SAR. The first approach is based on the magnetic properties of MNPs, whereas the second method is based on their thermodynamic (calorimetric) properties. In a recent review [92], the experimental methods to measure SAR were discussed along with the possible uncertainties. Comparison between magnetic methods and calorimetric methods were also discussed. Here, we focus on the calorimetric methods.

Thermodynamic properties of MNPs (or any material) are not easy to be measured since they should be done in thermal equilibrium. To minimize external heat transfer, measurements of heating power of MNPs should be done in adiabatic conditions which are not easy to achieve. Most of calorimetric experiments using MNPs are done in nonadiabatic conditions, and thus result in appreciable errors [92–94]. Thus, there are always some inaccuracies in such measurements and results should be carefully discussed.

However, because of the difficulty to build efficient adiabatic measurement systems and because the measurements in such systems are time-consuming, the SAR measurements are usually conducted in nonadiabatic conditions which results in some errors. It was suggested that accurate SAR measurements can be made using nonadiabatic conditions by using suitable experimental and analytical methods where heat losses from the nonadiabatic setup are accounted for [94]. Possible sources of the inaccuracy in in nonadiabatic SAR measurement are (a) the spatial inhomogeneity of temperature in the sample where the location of the thermal probe in the sample becomes important, (b) the delaying of heating since it takes some time for the heating curve to take off after the start of the heating process, (c) the change of heat capacity with temperature, (d) the inhomogeneity of the magnetic field through the volume of the sample, and (e) heating due to the experimental set-up itself (peripheral heating) and not due to heated MNPs.

In calorimetric experiments, an AMF is applied to the sample of MNPs and the variation of temperature is measured with time. The SAR is usually obtained from the initial slope of the (temperature–time curve) measured data using this equation.

The induced increase in the temperature of the water dispersion enables us to calculate SAR using Equation (12),

$$SAR\ (W/g) = \frac{C}{m_{MNP}}\frac{dT}{dt} \tag{12}$$

where C (in J/K) is the heat capacity of the sample (which includes the MNPs and the suspending medium), m_{MNP} is the mass (in g) of the MNPs in the sample, and $\frac{dT}{dt}$ is the initial slope of the temperature–time curve. The heat capacity of the sample is the sum of the specific heat multiplied by the mass of the components of the sample. For example, if the MNPs are suspended in water, the heat capacity of the sample will be $C = c_{MNP}m_{MNP} + c_{water}m_{water}$, where c_{MNP} and c_{water} are the specific heat values for the MNPs and the water, respectively, and m_{water} is the mass of the water in the sample [95]. The rationale behind the use of the "initial slope" method relies on three assumptions at the very initial stage of heating (a) heat transfer between the sample and the environment does not exist yet and thus adiabatic conditions are applicable, (b) temperature variations within the sample are very small and thus can be ignored, and (c) constant temperature approximations of heat transport properties results in very small errors and thus can be valid [96–99].

This "initial slope" method depends only on the initial temperature changes and ignores the entire heating curve and thus it does not display the entire temperature dependence of SAR [100]. In addition, it was shown that fluctuations and non-linear temperature rise can occur in the initial heating stage [96,101], which contradicts the main assumption of the initial slope method. This commonly used initial slope method was suggested to underestimate values by up to 25% [94]. The full-curve fit method was found to improve upon the "initial slope" method, but underestimation by up to 10% could result. A third method, the "corrected slope" method [94], was found to be the most accurate method. More details about several proposed methods to calculate SAR from heating data can be found in [92,94,101]. In [98], the validity of measured trends of SAR values with varied experimental conditions was discussed. The SAR values for obtained for magnetic nanoparticles depends on the geometry, saturation magnetization, coating used for functionalization, and parameters of ac magnetic field used for the measurements.

SAR values for of several ferrite nanoparticle systems are listed in Table 1.

Table 1. Specific absorption rate (SAR) values of ferrite nanoparticles with respect to size, shape, surface coating, and parameters used for obtaining hyperthermia measurements.

Shape & Size (nm)	Material	Coating	(kA/m) Field	Frequency (kHz)	(W/g) SAR	Reference
Octahedral-43	Fe_3O_4	CTAB	63	358	2483	[102]
Rings-73	Fe_3O_4	mPEG	35	400	2213	[103]
Disc-225	Fe_3O_4	CTAB	47.8	488	5000	[104]
Cubes-19	Fe_3O_4	PEG	29	520	2452	[48]
Sphere-14	$MnFe_2O_4$	GO	60	240	1588	[105]
Core–shell	$CoFe_2O_4$ @$MnFe_2O_4$	DMSA	37.3	500	2250	[41]
Nanoclusters-33	Fe_3O_4	PMA	23.8	302	253	[106]
Sphere-45	Fe_3O_4	GO	32.5	400	5160	[107]
Sphere-45	Fe_3O_4	PVP	32.5	400	1100	[107]

6. Thermometry in Magnetic Hyperthermia

For in vivo hyperthermia, the temperature of the targeted tissue or cells must be measured accurately using noninvasive methods. Tracking the temperature change in the tissue is important during the whole hyperthermia experiment, because a large increase in the temperature could cause damage to healthy cells. On the other hand, low temperatures of the tissue will not result in the required amount of heat to kill tumor cells. Several thermometry methods in magnetic hyperthermia are being investigated. The most used thermometry method is based on optical fibers. This method is being used mainly in hyperthermia in aqueous suspension and in vitro experiments. This method has two main limitations: (a) it cannot provide a detailed scan of temperature within the sample because the dimensions of the fiber tip are larger (~200 µm) [67], and (b) it is an invasive technique which is not preferred for in vivo applications. Noninvasive thermometry methods that depend on optical properties were investigated [108,109]. However, as these methods depend on properties of the light they face the limitation of short penetration depth into tissues. One of the good noninvasive thermometry method is based on magnetic resonance imaging (MRI) technique [110]. When conducting the magnetic hyperthermia treatment, the tumor tissue is placed at the center of the coil generating the AMF, whereas MRI thermometry requires the placement of the tumor tissue at the center of the MRI cavity. However, MRI uses high constant magnetic field (usually 3 T), which can pin the magnetic moments of MNPs and prevent them from rotating while they are exposed also to the AMF of hyperthermia. This will lead to a narrow dynamic hysteresis loops and thus will slow down heat generation of the MNPs in the hyperthermia process [111,112]. Thus, MRI thermometry might not be the optimum choice of thermometry in hyperthermia treatment. Several other noninvasive methods which depend on the magnetic response of MNPs to the applied magnetic field were proposed [113–122]. In these methods, the temperature-dependent of coercively [117,123], the temperature-dependent of magnetization, and the higher-order harmonics of the magnetization of MNPs were used as temperature sensors. In these noninvasive methods, the MNPs will do the heating and at the same time will work as a temperature probe.

7. Multifunctional Hybrid Magnetic Nanoparticles for hyperthermia Based Biomedical Applications

Magnetic nanoparticles with efficient heating capacity are subjected to intense research for various thermal based in vivo and in vitro studies for biomedical applications [124,125]. There are numerous reports of the detailed investigations for the applications of magnetic nanoparticles for magnetic imaging guided hyperthermia, magnetic actuated drug delivery, thermal cancer therapy, and biofilm eradication [126]. Magnetic nanoparticle when combined with materials like graphene oxide (GO), photoactive materials, mesoporous silica nanoparticles, and polymeric nanoparticles results in hybrid materials with multifunctionality [126–128]. Schematic representation of various phenomena involved in magnetic hyperthermia, thermosensitive drug delivery, and biomedical applications using magnetic nanoparticles are shown in Figure 1 [129].

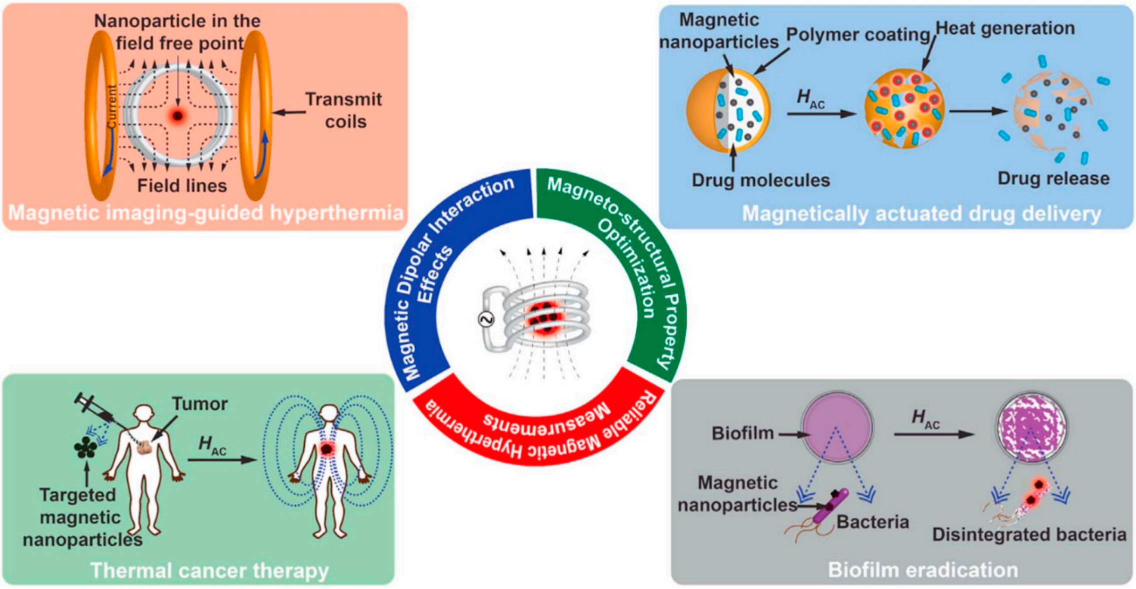

Figure 1. Schematic illustration of multifunctional ability of magnetic nanoparticles for various types of biomedical magnetic hyperthermia applications and parameters affecting the efficiency of magnetic hyperthermia treatment (reproduced with permission from Science Direct 2016) [129].

7.1. Graphene oxide-Fe_3O_4 Nanocomposites for Hyperthermia

Graphene oxide-Fe_3O_4 nanoparticle-based nanocomposites are widely investigated for various biomedical applications like drug delivery, magnetic hyperthermia, and MRI (Magnetic Resonance Imaging) contrast agents [130]. The unique chemical and physical properties of graphene oxide-based nanocomposites enable designing nanocomposites as per the requirement of physiological system. The presence of –OH, –COOH, and –CHO functional groups renders the easy attachment and release of various anticancer drugs [131]. The anticancer drugs usually delivered using graphene oxide-based composites as carrier vehicle, by change of pH or local heating via hyperthermia [132]. There are various studies where graphene oxide-based composites are considered for diagnosis and treatment of cancer. The first comprehensive report of graphene oxide-ferrite nanocomposite for magnetic hyperthermia was reported by Peng et al. [105]. They have reported the synthesis of hydrophobic ferrite nanoparticles attached to GO sheets using oleylamine as intermediary resulting in water dispersible MFNPs/GO nanocomposites. MGONCs-4 and MGONCs-4-PEG water dispersions were subjected to ac magnetic field, time-dependent temperature curves of MGONCs-4 and MGONCs-4-PEG were shown in Figure 2. From the magneto thermic data, it is evident that the heating rate of MGONCs-4-PEG was relatively lower than MGONCs-4. The difference in the heating rate could be explained by the presence of long-chain polyethylene glycol (PEG) which significantly altered the heating conduction. The field-dependent SAR values (Figure 2c) showed that the calculated SAR value of MGONCs-4 was greater than that of MGONCs-4-PEG. The SAR values of MGONCs-4 and MGONCs-4-PEG are 1541.6 and 1108.9 Wg^{-1} respectively. This finding is in good agreement with the other reported surface coating effects in which the heating capability would be hindered as the surface coating increases due to the suppression of the Brownian relaxation processes [133].

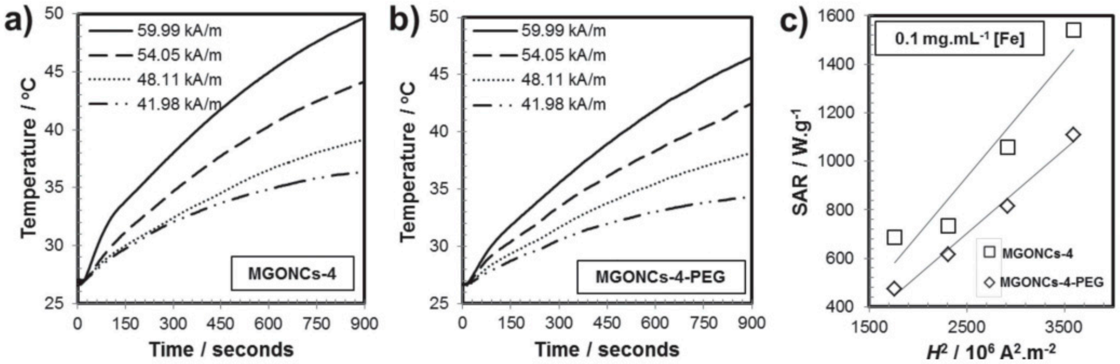

Figure 2. Magneto thermic data of water dispersions of (**a**) MGONCs-4 and (**b**) MGONCs-4-PEG treated with alternating magnetic field (AMF) (41.98–59.99 kAm^{-1}) at 240 kHz frequency. (**c**) Field-dependent SAR values of nanocomposite dispersions (reproduced with permission from Wiley Online Library 2012) [105].

Sugumaran et al. reported a GO-iron oxide-based nanocomposite system consisting of 45 nm nanoparticles grafted on GO sheet with very high SAR value [107]. They were able to achieve a SAR value of 5020 Wg^{-1} with alternating magnetic field of 400 kHz and 32.5 kAm^{-1}. Peng et al. have also studied the T_2-weighted MR imaging contrast enhancing ability of GO-ferrite nanocomposites. GO-ferrite nanoparticle system showed a high T_2 relaxation rate as 64.47 s^{-1} (with r_2 relaxivity value of 256.2 Fe mM^{-1} s^{-1}) with the MGONCs-4 with the iron concentration as low as 0.25 mM Fe. These results suggested that the presence of the aggregation of MFNPs on GO could provide additional enhancement of relaxation of water protons. The aggregation effect on relaxation process observed is further confirmed by the other reports [134]. The aggregation of ferrite nanoparticles leads to higher magnetic inhomogeneity in the water dispersion which causes the decrease in the transverse relaxivity of water protons. The graphene oxide framework of the composite provides an addition advantage of attaching water insoluble anticancer drugs and releasing them at the site of interest.

Sugumaran et al. have reported an in vivo magnetic hyperthermia studies for targeting of tumor bearing mouse model using PEGylated GO-IONPs [107]. Tumors were induced in mice by injecting 4T1 cancer cells into the mammary pads of mice. The mice with tumor volumes of approximately 100 mm^3 were treated with PEGylated GO-IONPs (Fe dose of 1 mg/cm^3) with PBS, PEG-GO-IONP under magnetic field. Mice tumors are subjected to AMF with 400 kHz frequency and a magnetic field of 32 kA/m for 10 min. Body weights and tumor volumes subjected to various conditions are shown in Figure 3. The mice injected with PBS or PEG-GO-IONP alone without AMF application and mice subjected to AMF alone, failed to suppress the growth of 4T1 tumor. The test group significantly inhibited the 4T1 tumor growth, indicating that the antitumor efficacies of PEG-GO-IONP mediated magnetic hyperthermia treatment were greater than that of either PEG-GO-IONP or AMF alone. The tumor treated under ac magnetic field with PEG-GO-IONP completely disappeared. In addition, no body weight loss (Figure 3d) was observed in the PEG-GO-NP-mediated magnetic hyperthermia treatment, indicating the relative safety of the treatment and tolerability of the administered dosage.

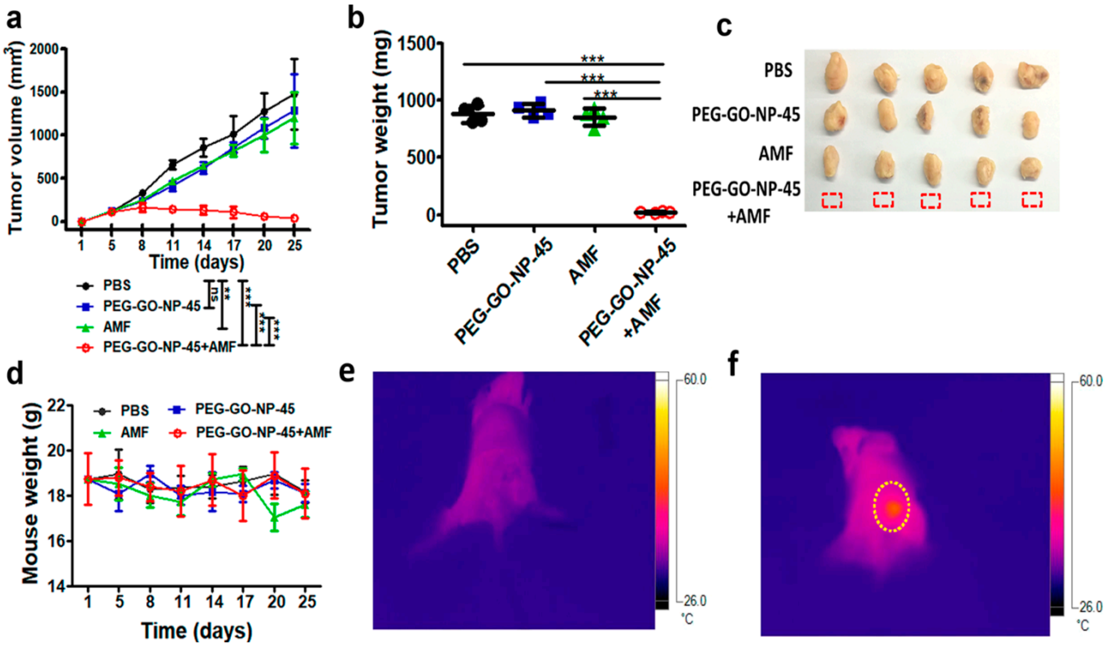

Figure 3. (**a**) Tumor volume versus days after the treatment with GO-NP and AMF. (**b**) Weights and (**c**) photographs of excised tumors at the end point for different treatment groups. (Tumor completely disappeared after hyperthermia treatment with PEG-GO-NP-45.) (**d**) Mouse weight after the treatments. Thermal images showing the temperature at the site of tumor and entire body of mouse during hyperthermia treatment: (**e**) control and (**f**) PEG-GO-NP-45+AMF (reproduced with permission from American Chemical Society 2019) [107].

7.2. Magnetic Nanogels for Thermosensitive Drug Delivery

Thermosensitive drug delivery agents are polymeric micelles which are synthesized using thermo-responsive polymers. These magnanogels are formulated using self-assembly process of amphiphilic block-copolymer [135]. Magnanogels are class of thermosensitive materials which are activated by ac magnetic field, formulation of these nanoparticles was reported in detail by several studies [136,137]. Nanogels are used in various biomedical applications like drug delivery systems, analytical and diagnostic devices, and thermal therapy [138]. These nanocarries are functionalized with target specific molecules, enabling differentiation between normal and tumor tissues [139]. Advances in material fabrication and designing enables to use of thermosensitive nanocarriers for controlled drug delivery in the future.

Nanogels were prepared in a batch reactor by conventional precipitation radical copolymerization of oligo(ethylene glycol) methyl ether methacrylate in water, without using any surfactants [140]. Magnetic nanoparticles were synthesized by chemical coprecipitation of ferrous and ferric ions in basic medium. To synthesize the magnanogel, a known quantity of nanogel is taken and pH is adjusted to 3.0 and magnetic nanoparticles are added drop wise into the nanogel solution under stirring at room temperature. The anticancer drug doxorubicin is attached to magnanogel in HEPS buffer solution under stirring for 24 h. The schematic of anticancer drug delivery using magnanogels is explained in Figure 4.

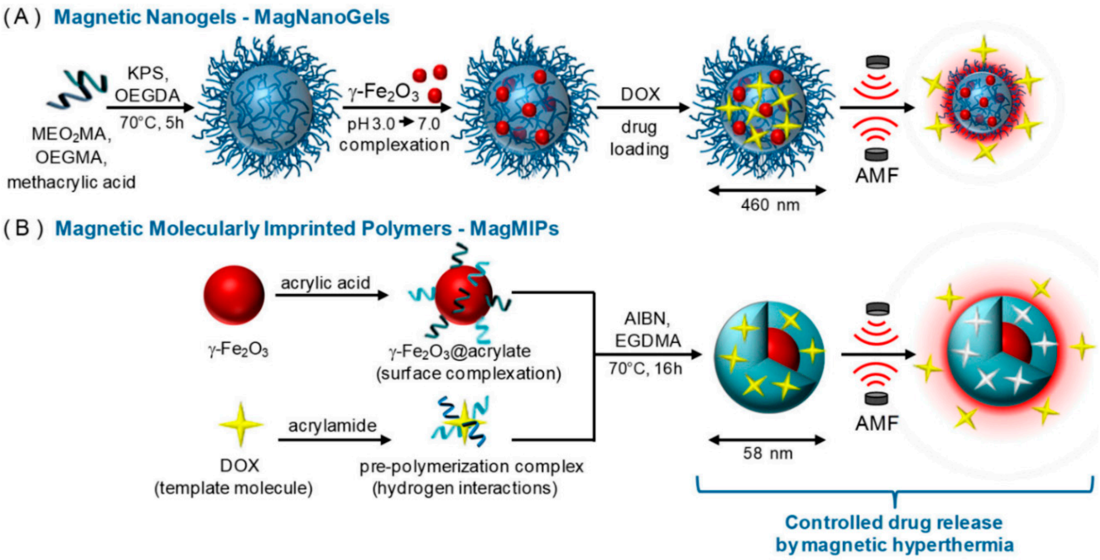

Figure 4. (**A**) Schematic illustration of the synthesis of magnanogels by radical copolymerization and post-assembly of MNPs inside nanogels and (**B**) synthesis of MagMIPs by grafting of acrylic acid compound in the surface of MNPs and the growth of the polymer in the presence of DOX for imprinting polymerization. Loading and release of DOX under an AMF (reproduced with permission from MDPI (open access) 2018) [141].

Intracellular DOX release experiments using magnanoels is reported by Esther et al. [140]. DOX release is stimulated by change of pH (internal stimulus) and externally applied AMF (external stimulus). DOX release is highly pH sensitive at pH 7.5 25% of DOX is released after 4 h whereas at pH 5.0 the release of DOX is increased to 96%. These results are in good agreement with other reported results of pH-sensitive nanogels functionalized with carboxylic acid groups [142,143]. Under the same pH conditions DOX release increased under ac magnetic field of 335 kHz and 12.0 $\mathrm{kAm^{-1}}$. These studies demonstrate that ac magnetic field helps in remotely trigger DOX release without macroscopic heating. The diameter of the magnanogels decreases under ac magnetic field due to the generated magnetic heat. The shrinkage facilitates the release of DOX at the site of interest. They have also studied in vitro DOX release in cancer cells (PC-3) using DOX-magnanogels. PC-3 cancer cells were treated with 15 and 10 pg of DOX-magnogels and DOX-Magnetic nanoparticles. The studies showed that the internalization did not cause any toxic cellular response, demonstrating the biocompatible nature of both nanogels and nanoparticles without DOX. Confocal images of cancer cells treated with DOX encapsulated magnanogels and magnetic nanoparticles were shown in Figure 5b. Cell viability was more impacted by the internalization of the magnanogels containing DOX than magnetic nanoparticles associated with DOX. These results confirm that the payload is continuously released from magnanogels, but can be delivered in larger amounts under AMF. By contrast, when DOX is bonded to the MIP, DOX is inactive. Internalization and DOX release experiments using magnanogels showed the efficiency under AMF due to local heating of the magnetic nanoparticles.

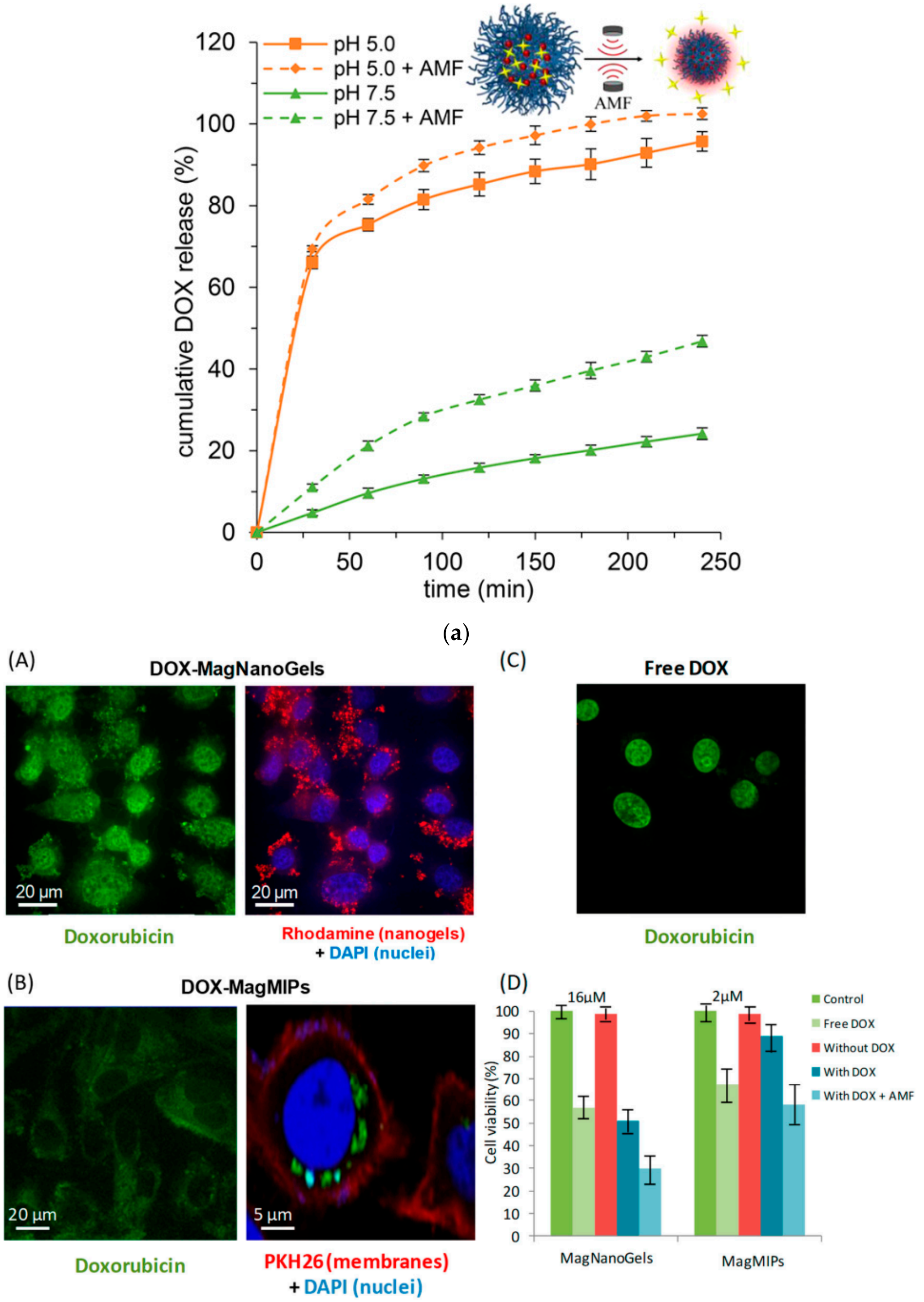

Figure 5. (**a**) DOX release profile (%) versus time under physiological conditions (pH 7.5, 0.1 M HEPES sodium) and acidic (pH 5.0, 0.05 M citric acid and 0.1 M sodium phosphate) at 37 °C without and with an AMF. (**b**) Confocal imaging of tumor cells (PC-3) having internalized: (A) Magnanogels and (B) DOX-MagMIPs nanoparticles. (C) Cells incubated for 2 h with free DOX (D) Cell viabilities for free DOX, DOX-magnanogels, and DOX-magnetic nanoparticles (reproduced with permission from American Chemical Society 2017) [140].

7.3. Magnetic Mesoporus Silica Nanoparticles for High Dose Delivery of Anticancer Drugs

Mesoporous silica nanoparticles (MSNs) have some unique advantage of large pore volume with uniform mesoporosity, biocompatibility, and biodegradation [144,145]. This unique property of silica nanoparticles renders high drug loading capacity. Conventional MSNs can load 200–300 mg of anticancer drug per 1 g of silica. However, MSNs with hollow core–mesoporous shell structure can achieve 1 g drug per 1 g silica [144,146]. Physical entrapment of anticancer drugs due to the hallow core–shell geometry prevents uncontrolled burst release or poor drug loading [147]. In addition, functionalization of MSNs with materials, such as magnetic nanoparticles, luminescent materials and polymers introduces the multifunctional modality of targeted dug delivery and imaging. The polymers attached to the core–shell nanoparticles act as thermosensitive gatekeepers for opening the pores and release the drug using ac magnetic field. Thamos et al. has reported a nanomotor based on MSPs with zinc doped ferrite nanoparticles in silica matrix [148]. These MSNPs were coated with temperature-sensitive copolymer of poly-ethyleneimine and n-isopropylacrylamide which acts as a gatekeeper and retains DOX into the polymer shell linked by electrostatic forces or hydrogen bonds [149]. Once these nanomotors are administrated into cancer cells motors were activated by applying ac magnetic field. This study shows that the polymer can be used as a gatekeeper for controlled drug delivery along with the thermic effect of magnetic nanoparticles. The schematic illustration of mesoporous silica-based nanomotors for drug delivery is shown in Figure 6.

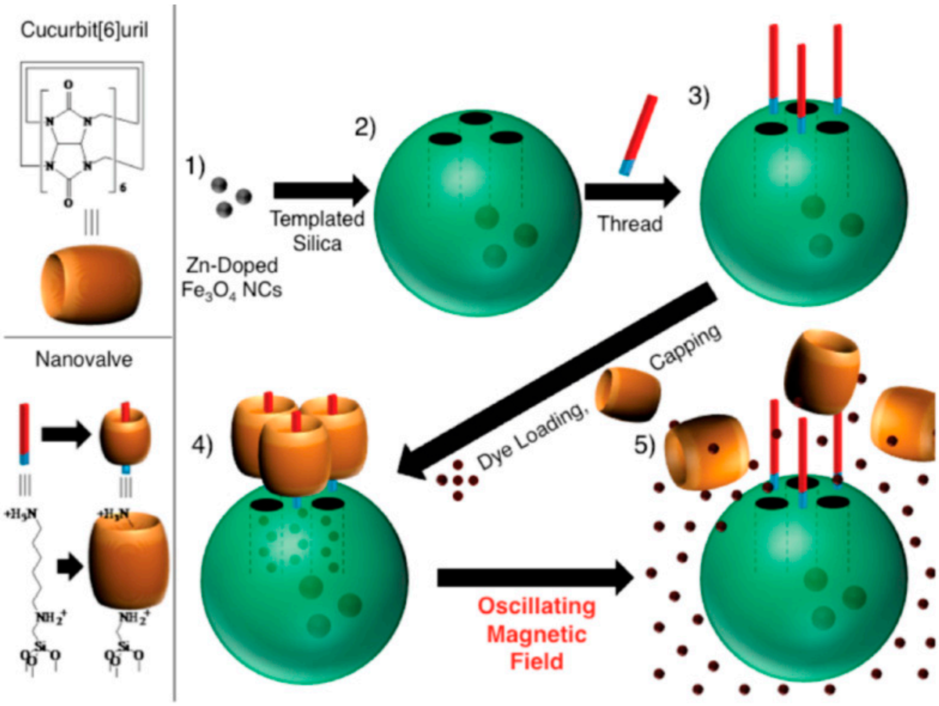

Figure 6. ZnNCs (1) are synthetically positioned at the core of the mesoporous silica nanoparticles (2). The base of the molecular machine is then attached to the nanoparticle surface (3). Drug is loaded into the particle and capped (4) to complete the system. Release can be realized using remote heating via the introduction of an oscillating magnetic field (5) (reproduced with permission from American Chemical Society 2010) [148].

Lee et al. has reported the synthesis of multifunctional nanocontainer with iron oxide and mesoporus silica and cyclodextran as gatekeeper [150]. They have estimated the pore size of the using Brunauer–Emmett–Teller (BET) nitrogen adsorption–desorption isotherms and Barrett–Joyner–Halenda (BJH). The pore diameter obtained is 2.5 nm and pore volume is 1.756 cm^3g^{-1}. Eduardo et al. reported the use of magnetic mesoporous core shell nanoparticles coated with thermoresponsive polymer (TRP) for in vitro drug release using magnetic field, the schematic illustration of the same is provided in

Figure 7 [151]. Magnetic nanoparticles used in this study were synthesized by simple coprecipitation method and stabilized by exadecyltrimethylammonium bromide (CTAB) in water medium. The surfaces of the nanoparticles were functionalized with polymerizable groups with 3-tris(trimethylsiloxy) prpyl methacrylate. The polymer shell has a lower critical solution temperature of 42 °C, which can be adjusted by altering the ratio between monomers. Below critical solution temperature the polymer chains forms a mesh which is useful to block the pores of mesoporous silica, which in turn helps hold the drug. Upon magnetic field treatment the polymer surface collapses and triggers drug release [152].

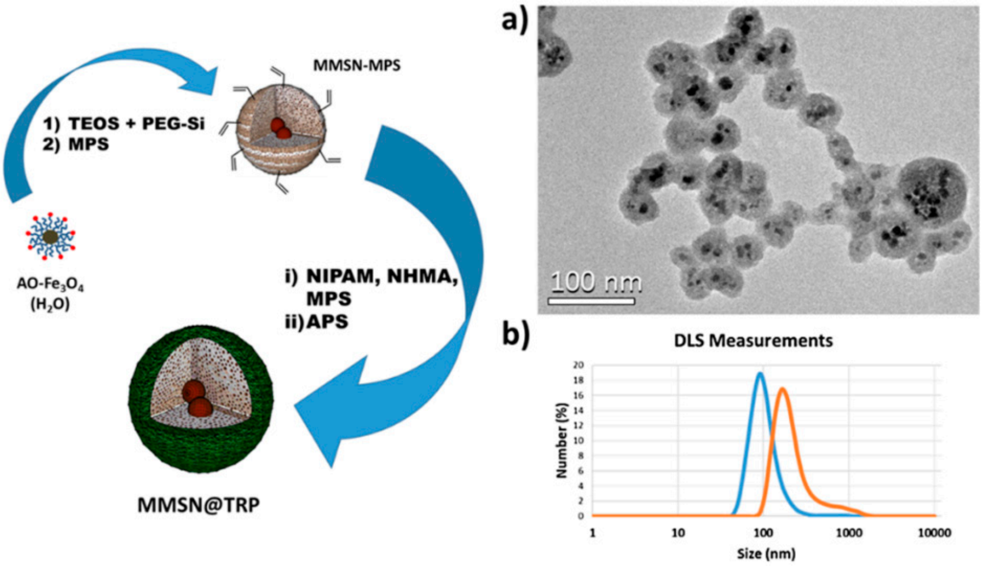

Figure 7. Schematic of the synthesis method of MMSN@TRP (thermo responsive polymer). (**a**) TEM image of the MMSNs coated with TRP (**b**) hydrodynamic size of the precursor (MMSN-nanoparticles, blue line) and the final nanocarrier (MMSN@TRP, orange line) (reproduced with permission from American Chemical Society 2018) [151].

7.4. Multifunctional Drug Delivery Agents Through Magnetic and Photothermal Therapy

Photoactive multifunctional magnetic nanoparticles are designed for the synergistic therapy of controlled drug release, magnetic hyperthermia, and photothermal therapy [153,154]. The combination of magnetic nanoparticles and photothermal agents can be directed magnetically to the site of interest (tumor), and their distribution in tumors and other organs can be imaged through MPI [155]. The controlled clustering of magnetic nanoparticles along with photothermal agents increases the molar adsorption coefficient in the near infrared region. The conversion efficiency of near-infrared (NIR) light energy into heat is also high for magnetic photothermal hybrid nanoparticles. The multifunctional magnetic composite consists of quantum dots as local photothermal generators and magnetic mesoporous silica nanoparticles (MMSN) or CQDs as drug carriers and magnetic nanoparticles as thermal seeds. The schematic illustration of hybrid composites for dual therapy is shown in Figure 8.

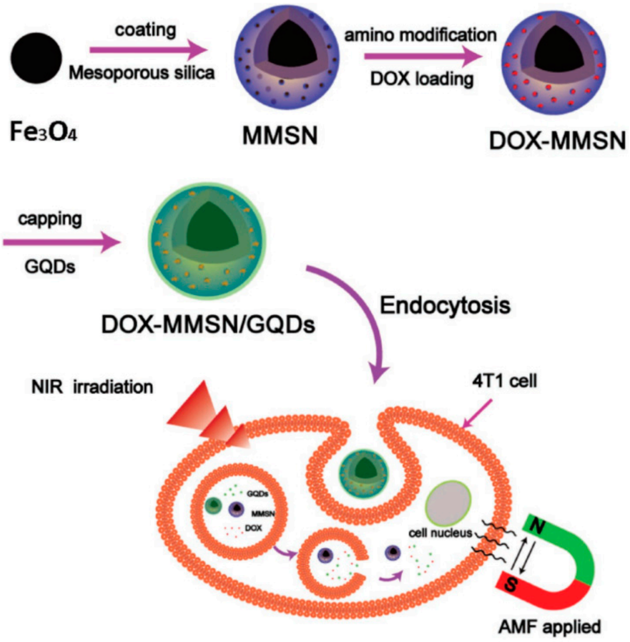

Figure 8. Schematic illustration of the synthesis of the DOX MMSN/GQDs nanoparticles and synergistic therapy combined with controlled drug release using magnetic hyperthermia and photothermal therapy (reproduced with permission from Wiley Online Library 2017) [156].

Yan et al. reported gold nanoshell-coated ferrite nanomicelles for MRI and light-induced drug delivery and photothermal therapy [157]. Nanomicelles possess improved drug loading capacity and good response to magnetic field for targeting the tumor. Nanomicelles show surface plasmon absorbance in the near infrared region (808 nm). Cancer cells incubated with gold-coated nanomicelles show good biocompatibility, and when treated with NIR and magnetic field they showed significant cytotoxicity. The thermal effects are synergic in nature. Heating profile and DOX releasing behavior is shown in Figure 9.

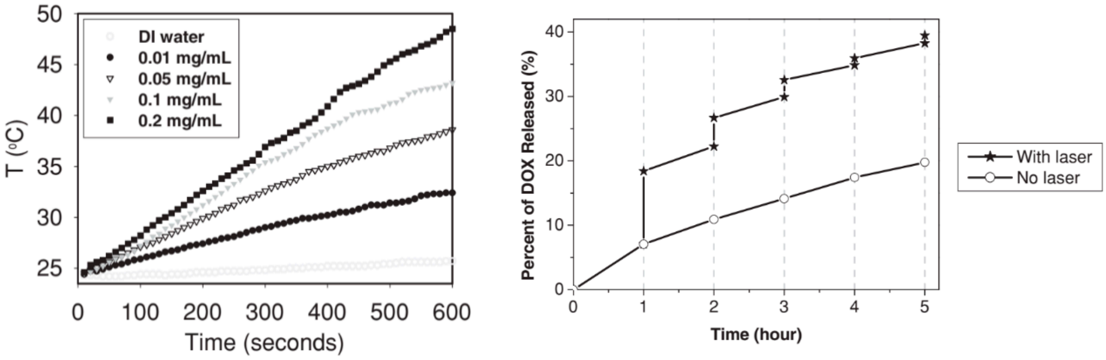

(**a**) (**b**)

Figure 9. (**a**) Temperature elevation in aqueous solutions containing CDF-Au-shell nanomicelles of different concentrations under night-infrared (NIR) laser irradiation (808 nm, 2 W) measured every 10 s using a digital thermometer, over a period of 10 min. (**b**) NIR-triggered release of DOX from CDF-Au-shell nanomicelles. (Reproduced with permission from Wiley Online Library 2013) [157].

Yoa et al. has reported the drug release behavior under the stimuli of magnetic hyperthermia and photothermal effect using magnetic mesoporous silica nanoparticles (MMSN/GQDs). Fe_3O_4 nanoparticles are prepared and encapsulated by mesoporous silica matrix to obtain Fe_3O_4/SiO_2 (MMSN). MMSN nanoparticles are spherical and the particles size is estimated to be approximately 100 nm. The obtained nanoparticles were modified with amino groups and GQDs with hydroxyl, epoxy, and carboxyl groups are used to cap the outlets of mesoporous channels for the formation of the DOX-MMSN/GQDs nanoparticles. GQDs prevent the DOX from leaking and uncontrolled burst of DOX at the site of off target. This is unique composite which can be used for the delivery of both water soluble and insoluble drug together. The organic nature of GQD frame work enables to attach water insoluble anticancer drugs. The magnetic and photo thermic heating efficiency of the MMSN/GQDs nanoparticles is shown in Figure 10. Temperature of the MMSN/GQDs suspension increased rapidly under AMF, and the temperature increase rate is concentration dependent. The specific absorption rate (SAR) value of the MMSN/GQDs nanoparticles was calculated as ~44 Wg^{-1}. MMSN/GQDs suspensions were irradiated under NIR laser irradiation (λ = 808 nm, 2.5 Wcm^{-2}). It visually confirmed the rapid temperature increase for the MMSN/GQDs suspension by NIR irradiation. MMSN/GQDs nanoparticles have the advantage of producing heat by dual methods that can be used for increasing the temperature in physiological systems, which helps kill cancer cells.

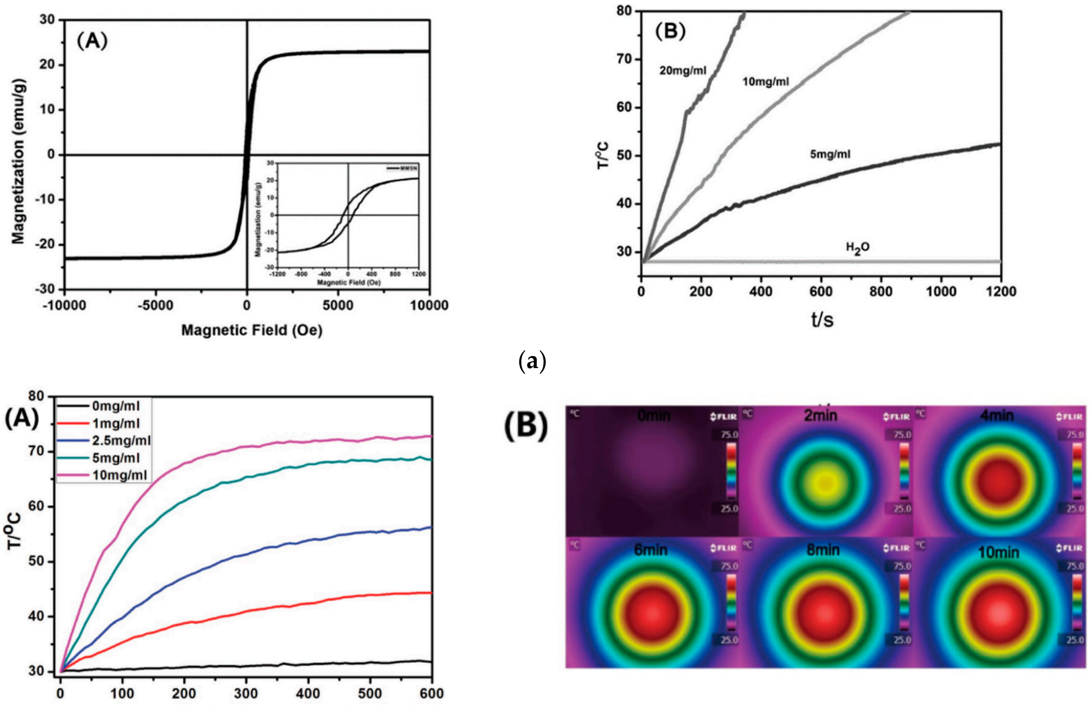

(**a**)

(**b**)

Figure 10. (**a**) (A) The magnetization curve of the MMSN/GQDs nanoparticles measured at 298 K. (B) Magnetic heating curves of the H_2O and MMSN/GQDs suspensions under an alternating magnetic field with a magnetic field strength of 180 G and frequency of 409 kHz. (**b**) (A) Photothermal heating curves of MMSN/GQDs suspension evaluated by 808 nm laser irradiation (2.5 Wcm^{-2}). (B) The infrared thermal images of the MMSN/GQDs suspension at a concentration of 10 mg mL^{-1} with 808 nm laser irradiation (reproduced with permission from Wiley Online Library 2017) [156].

Shawei et al. reported a multifunctional $NaYF_4$:Yb,Er@PE_3@Fe_3O_4 nanocomposite with superparamagnetic and photothermal performance. The multicomponent hybrid nanoparticles were synthesized by layer-by-layer self-assemble method. Compared to bare Fe_3O_4 nanoparticles, the multifunctional nanocomposites exhibited enhanced absorption at 808 nm and showed improved near-infrared photothermal effect. The fluorescent imaging sensitivity is increased when it is combined with magnetic field. The in vivo images of the mouse 4T1 breast cancer cells treated with hybrid nanoparticles in the presence of magnetic field and without magnetic field are shown in Figure 11a. The fluorescence images taken without magnetic field shows weak luminescent signals, whereas in the case magnetic field treated cells the up conversion signals are observed from the 4T1 cells. This demonstrates that the application of magnetic field for targeted drug delivery enhanced synergistic imaging sensitivity. Photothermal therapy ability of the $NaYF_4$:Yb,Er@PE_3@Fe_3O_4 nanocomposites for killing 4T1 cancer cells is shown in Figure 11b. The cell viability results show that hybrid nanocomposite treated with external magnetic field is highly effective for killing of cancer cells. The reasons might be cancer cells were pushed close to the photothermal agents under the external magnetic field.

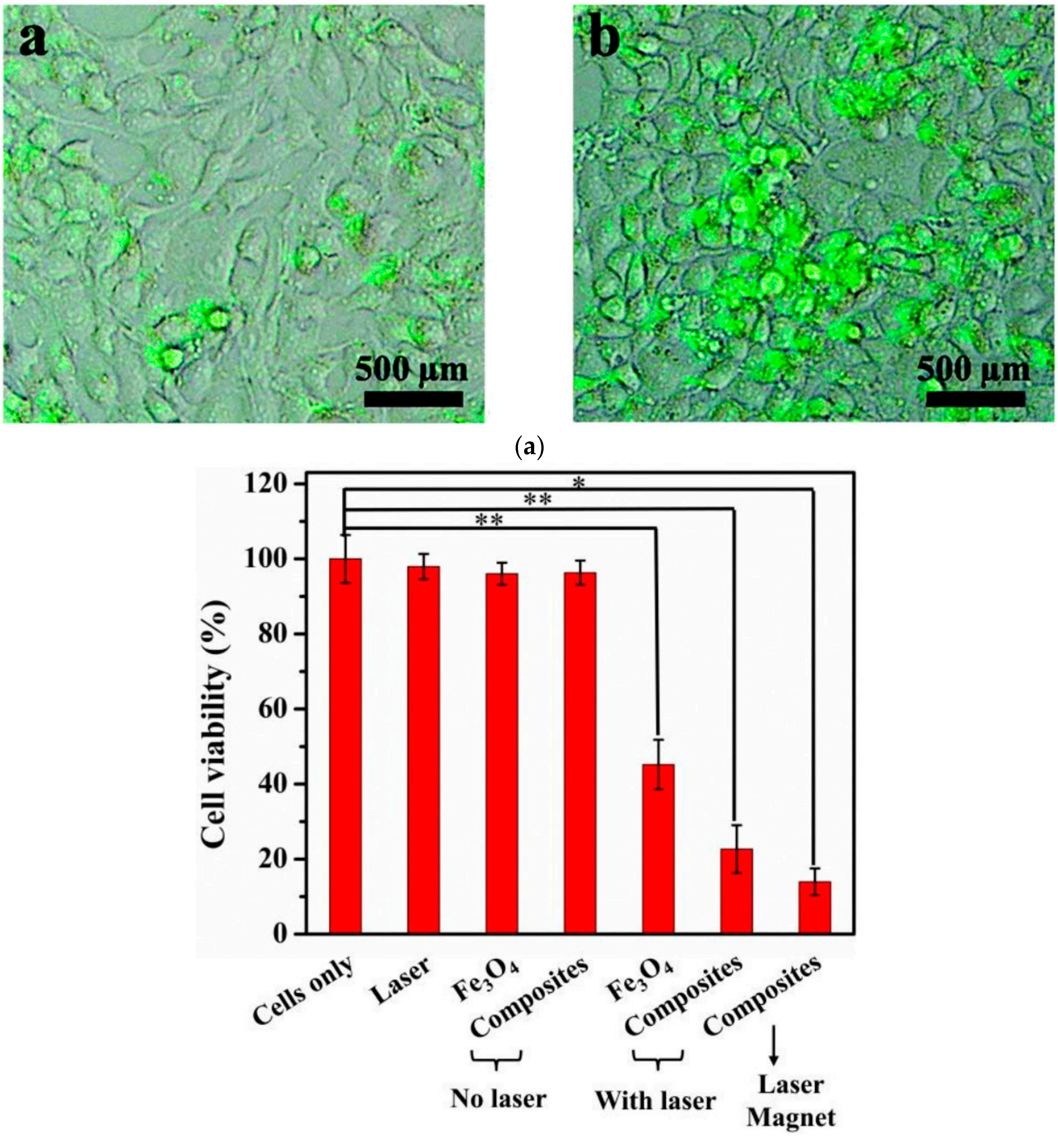

(**a**)

(**b**)

Figure 11. (**a**) The fluorescence images of 4T1 cells after incubating with $NaYF_4$: Yb, Er@PE_3@Fe_3O_4 nanocomposites (A) without or (B) with external magnetic field. (**b**) Viabilities of the mouse 4T1 breast cancer cells treated with hybrid nanoparticles under various conditions. Error bars were based on standard deviations, * $p < 0.05$ and ** $p < 0.01$. (Reproduced with permission from Royal Society of Chemistry 2019) [158].

7.5. Magnetic Particle Imaging and Hyperthermia in Vivo Applications

Magnetic particle imaging (MPI) is a new tomographic technique developed in the early 2000 [159]. MPI is tracer tracking technique that allows tracking and quantification of the signal from tracer magnetic nanoparticles [160]. MPI gives quantitative 3D information of the region of the interest with high spatial and temporal resolution which helps in real-time high resolution in vivo imaging. As a tracer tracking technique MPI may lead to the new possibility of 3D in vivo real-time imaging which will be of great help for real time treatment and imaging [161], human scanners will become available in a few years. The tracer used in the MPI imaging is usually superparamagnetic nanoparticles; this also adds additional advantage as iron oxide nanoparticles are well investigated for MRI contrast agents and their behavior in physiological environments is thoroughly understood [162]. Image-guided treatment of tumors enables physicians to localize the treatment with great precision and minimal damage to the healthy tissue. More details of the instrumentation and working principles can be found in the recently published review reports [9].

Tay et al. has reported the in vivo studies of magnetic hyperthermia treatment and magnetic particle image-guided modality [163]. This study demonstrated theranostic investigation of quantitative MP image-guided treatment using spatial localization of magnetic hyperthermia to arbitrarily selected organs. This addresses a key challenge of conventional magnetic hyperthermia affecting off-target organs causing collateral heat damage. Superparamagnetic iron oxide nanoparticles were injected to the tumor site and subjected to ac magnetic field. During MPI scan, negligible heating was observed in the mouse when it is subjected low frequency (20 kHz). During a high-frequency (354 kHz) heating scan without MPI gradients, all in vivo locations with nanoparticles heat up, damaging the healthy liver. When the MPI gradients are used, only the tumor is heated while the liver is spared. Dual tumor mouse was used to demonstrate arbitrary user-control of which tumor to heat. Only the bottom tumor heated up while the top tumor was spared. Only the top tumor heated up while the bottom tumor was spared, demonstrating arbitrary control of the site of heating just by shifting the MPI field-free line. The results shown in Figure 12 for the experimental MPI guided hyperthermia confirm that localization is achieved in vivo. A control mouse with saline instead of SPIONs was also subjected to the same uniform AMF but showed no increase in tumor and liver temperatures, verifying that this indiscriminate heating is not a result of nonspecific SAR from AMF interacting with biological tissue. These studies show that, with MPI gradients, the user can arbitrarily control the location of heating. With guidance from the initial MPI image, the treatment planning can design a heating to avoid collateral damage to healthy tissue.

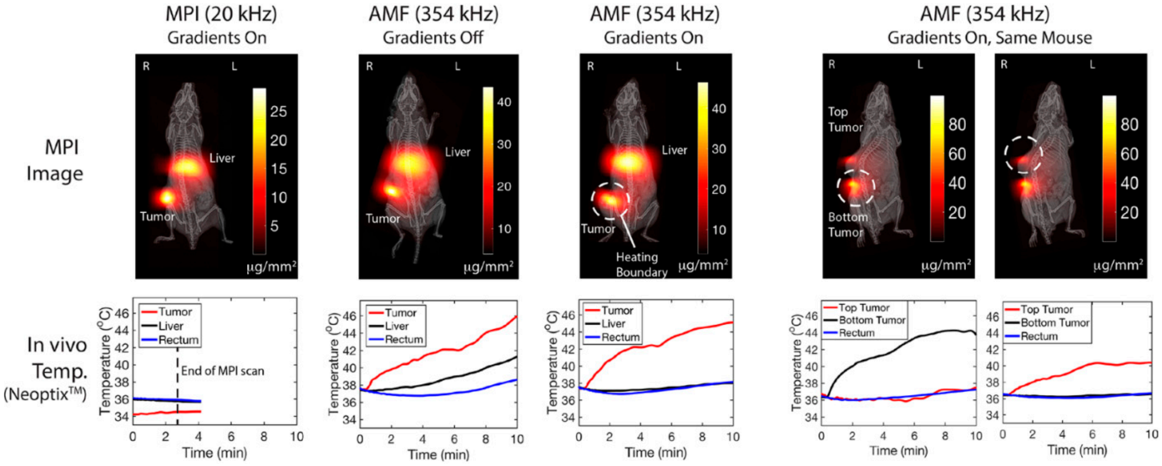

Figure 12. In vivo experimental demonstration of localization of magnetic hyperthermia. All in vivo local temperatures were measured by Neoptix fiber optic temperature sensors (reproduced with permission from American Chemical Society 2018) [163].

8. Synthesis of IONPs

It is well known that MNP synthesis method has a significant role in determining MNP magnetic properties, and thus their SAR values [164]. However, the synthesis mechanisms needed to produce well controlled magnetic properties are not well established. Here, we present several synthesis methods that are currently being used to produce IONPs. Various approaches such as wet chemical [165–167], template-directed [168,169], microemulsion [170–172], thermal decomposition [172,173], solvothermal method [174,175], solid state [176,177], deposition method [178], spray pyrolysis [179,180], self-assembly [181], physical, and lithographic [182,183] techniques have been extensively used for the synthesis of a wide variety of magnetic nanoparticles including iron oxide, metal, metal alloys and core–shell and composites structures. However, a comprehensive review of various synthetic techniques, and we will give a short description of only those methods that offer excellent size and shape control.

8.1. Thermal Decomposition

This method of synthesis involves the chemical decomposition of the substance at elevated temperature. During this method the breaking of the chemical bond takes place. This method of synthesis for magnetic nanostructures mostly use organometallic compounds such as acetylacetonates in organic solvents (benzyl ether, ethylenediamine, and carbonyls) with surfactants such as oleic acid, oleylamine, polyvinyl pyrrolidone (PVP)**,** cetyltrimethyl ammonium bromide (CTAB), and hexadecylamine. In this method the composition of various precursors that are involved in the reaction determine the final size and morphology of the magnetic nanostructures. Peng et al. and co-workers used the thermal decomposition approach for controlled synthesis (in term of size and shape) of magnetic oxide [184]. Using this method, nanocrystals with very narrow-sized distribution (4–45 nm) could be synthesized along with the excellent control of morphology (spherical particles, cubes). When thermal decomposition method is used, iron oxide nano particles with excellent control of size, morphology and good crystallinity have been resultantly fabricated by Alivisatos and co-workers [185]. The preparation of magnetic nanoparticles for applications in biomedicine have fabricated maghemite nanocrystals with size of 3–9 nm by thermal decomposition of FeCup3 (Cup: *N*-nitrosophenylhydroxylamine) at 250–300 °C, as shown in Figure 13. Recently, Sun and Zeng et al. [186] have demonstrated the fabrication of monodisperse magnetite nanoparticles with size ranges of 2–20 nm by decomposition of iron (III) acetyl acetone at 260 °C in the presence of benzyl ether, oleic acid, and oleyl amine. In a more recent study, Nogues and co-workers have synthesized highly mono disperse cubic and spherical maghemite (Fe_2O_3) nanocrystals by using thermal decomposition method [187], as shown in Figure 14. The ratio of precursors and the thermal decomposition time can be used to achieve size and morphology controlled nanocrystals.

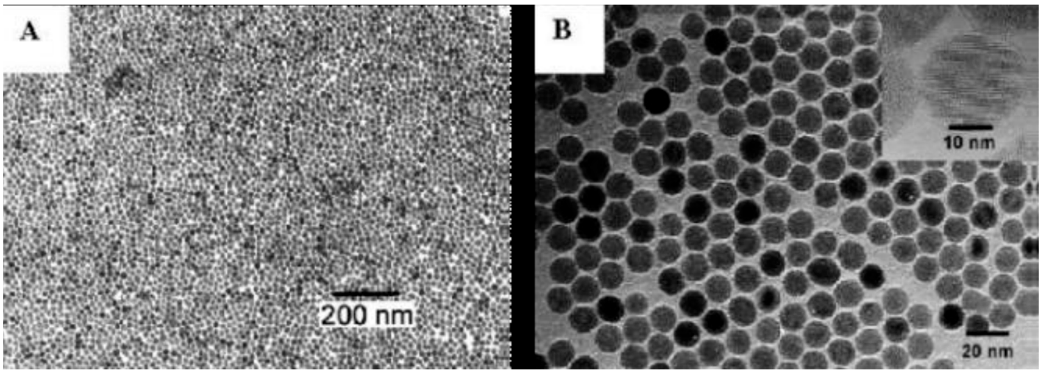

Figure 13. Maghemite nanoparticles prepared by thermal decomposition of Iron precursors: (**A**) $FeCup_3$ and (**B**) $Fe(CO)_5$ (reproduced with permission from American Chemical Society 1999) [185].

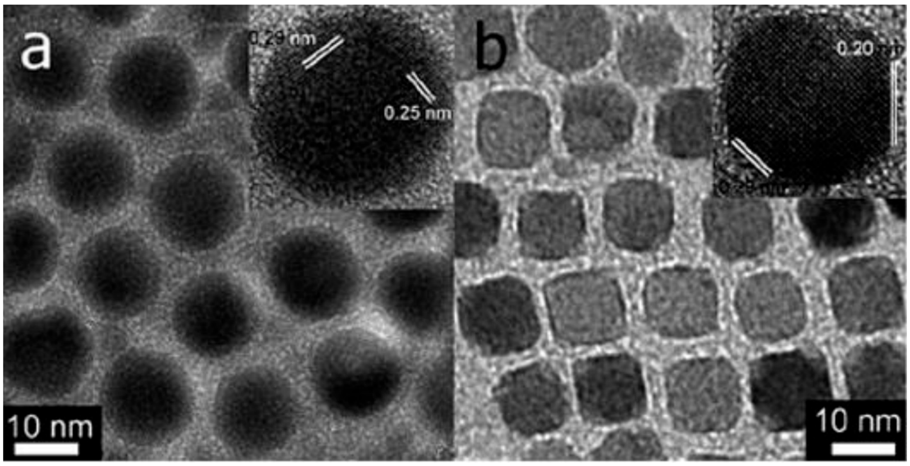

Figure 14. High-resolution TEM images showing the monodisperse (**a**) nanosphere and (**b**) nanocubes achieved by thermal decomposition method (reproduced with permission from American Chemical Society 2006) [187].

Nogues et al. showed that short decomposition duration (2–4 h) resulted in spherical whereas longer duration (10–12 h) resulted in cubic morphology. The technique of thermal decomposition was not only used for synthesis of metal oxide magnetic nanocrystals but metal magnetic nanoparticles of transition metals (Co, Ni, and Fe) were also synthesized through introducing a reducing agent into a hot solution of metal precursor and surfactant [26]. With precise control of the temperature and ratio of metal precursor to surfactant, MNPs with the control size and shape were synthesized.

8.2. Hydrothermal Synthesis

Another important chemical synthesis technique that involves the use of liquid–solid–solution (LSS) reaction and gives excellent control over the size and shape of the MNPs is the hydrothermal synthesis. This method involves the synthesis of MNPs from high boiling point aqueous solution at high vapor pressure. It is a unique approach for the fabrication of metal, metal oxide [188,189], rare earth transition metal magnetic nanocrystals [190], semiconducting [191], dielectric, rare earth fluorescent, and polymeric [192]. This synthetic technique involved the fabrication of magnetic metallic nanocrystals at different reactions conditions. The reaction strategy is based upon the phase separation which occurs at the interface of solid–liquid–solution phases present in the reaction. For example, the fabrication of monodisperse (6, 10 and 12 nm) Fe_3O_4 and MFe_2O_4 nanocrystals is demonstrated by Sun et al. and co-worker [193]. Wuwei and co-worker have synthesized oblique and truncated nanocubes of α-Fe_2O_3 by one step facile hydrothermal method. This group studied the effect of volume ratio of oleylamine and acetylacetone for the fabrication of α-Fe_2O_3 with two different morphologies as shown in Figure 15. The synthesize magnetic nanoparticles were used for photocatalytic degradation of organic dye, and it was observed that truncated nanocubes possess much higher photocatalytic degradation activity as compared to oblique nanocubes [194].

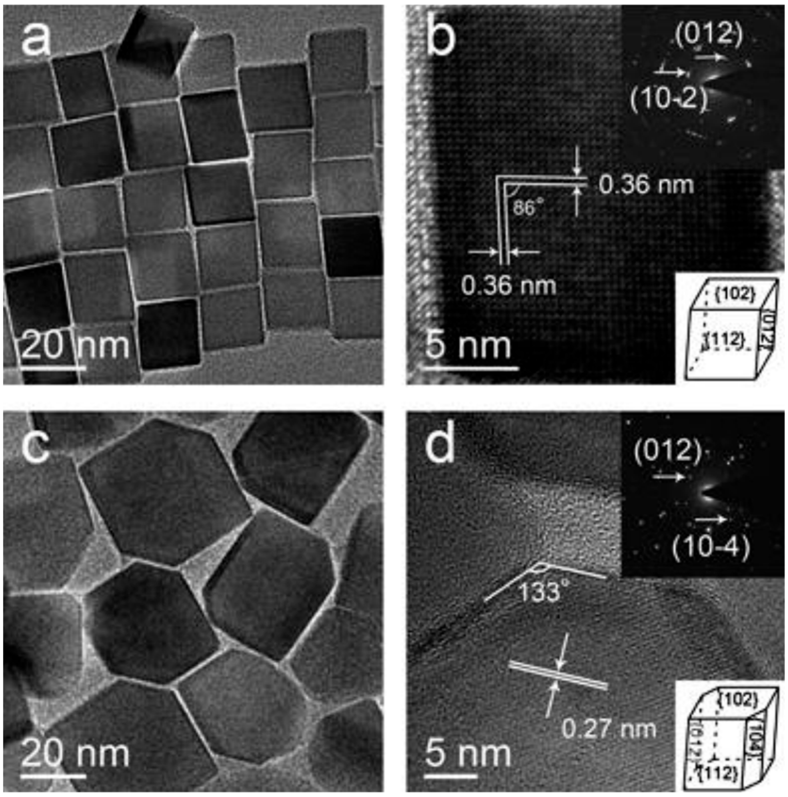

Figure 15. (**a**) TEM image of oblique nanocubes, (**b**) HRTEM image, FFT pattern and geometrical model of oblique nanocubes, (**c**) TEM image of truncated nanocubes, and (**d**) HRTEM image, FFT pattern and geometrical model of truncated nanocubes (reproduced with permission from Royal Society of Chemistry 2013) [194].

The mechanism of formation of the α-Fe_2O_3 nanoparticles with oblique and truncated morphology is given below in Figure 16. The main cause of formation of two different morphologies is the presence of oleic acid. The presence of oleic acid led to the formation of oblique nanocubes, whereas truncated nanocubes are formed in the absence of oleic acid.

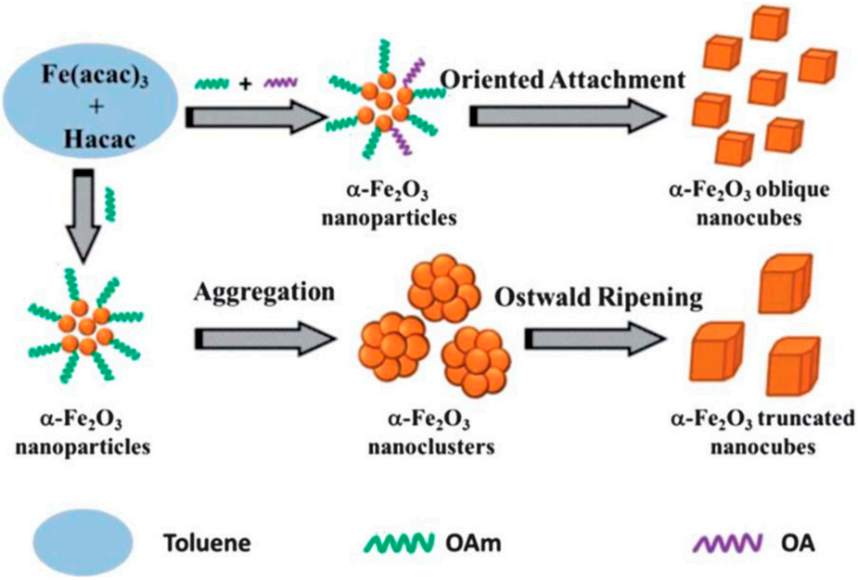

Figure 16. Mechanism of formation of oblique and truncated nanocubes (reproduced with permission from Royal Society of Chemistry 2013) [194].

Zeng et al. have synthesized novel Fe_3O_4 nanoprism by a hydrothermal process using oleylamine (OAm) both as surfactant and reducing agent. The synthesized Fe_3O_4 exposed two kinds of crystal planes (111) and (220), as shown in Figure 17 [195].

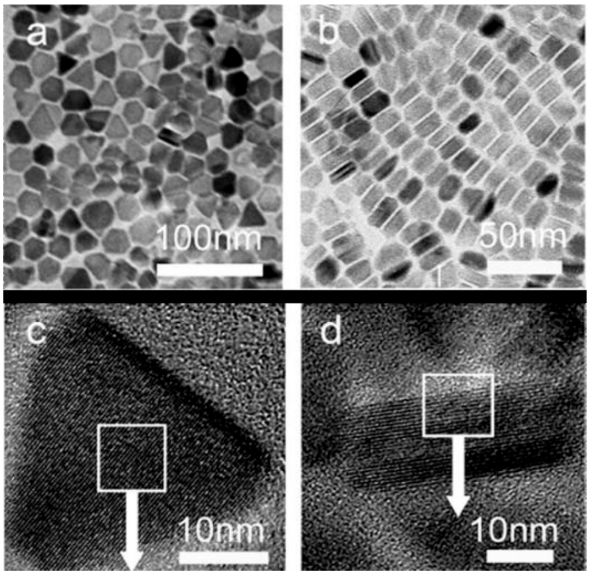

Figure 17. TEM images of Fe_3O_4 nanoprisms (**a**) lying flat and (**b**) self- assembled on the substrates (**c**), and (**d**) HRTEM images of Fe_3O_4 nanoprisms with a spacing of 0.301 nm (reproduced with permission from Royal Society of Chemistry 2010) [195].

They experimentally proved the crystal plane dependent electrochemical activities of nanoprism as clear from Figure 18b. Oleylamine was found to plays key role in the formation of different planes Fe_3O_4 nanoprism, because the amine group of oleylamine absorb at certain planes and slows their growth while allowing the growth of other planes leading to different morphology.

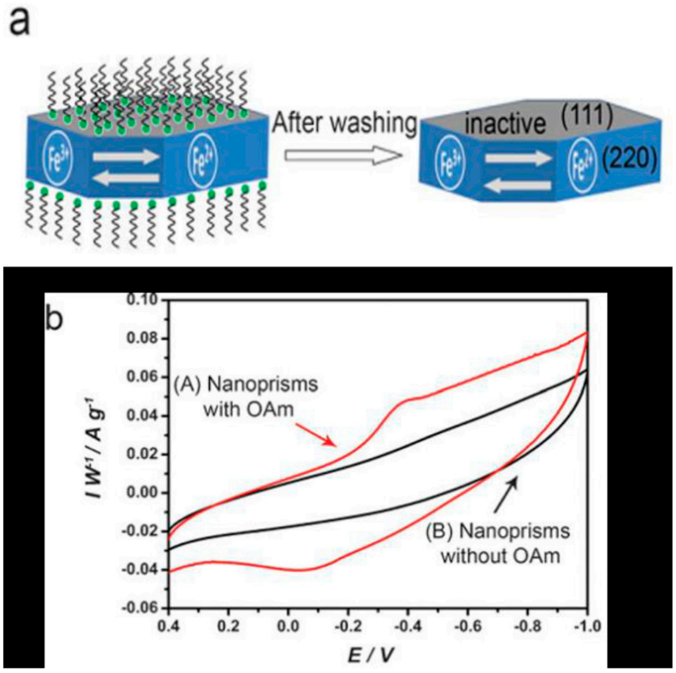

Figure 18. (**a**) Schematic illustration of Fe_3O_4 nanoprisms redox reaction. (**b**) Cyclic voltammograms of electrodes made of (A) Fe_3O_4 nanoprism with OAm (B) Fe_3O_4 nanoprisms without OAm in 1 M Na_2SO_3 (reproduced with permission from Wiley Online Library 2006) [195].

8.3. Microwave-Assisted Synthesis

Microwave-assisted method is a chemical method that use microwave radiation for heating materials containing electrical charges for instance polar molecule in the solvent or charge ion in the solid. Compared with other heating methods, microwave-assisted solution fabrication methods have got more focus of research because of rapid processing, high reaction rate, reduce reaction time, and high yield of product. Wang reported the synthesis of cubical spinal MFe_2O_4 (M = Co, Mn, Ni) high crystalline structure in a short time of just 10 min by exposure the precursors to microwave radiation [196] shown in Figure 19; they also used the microwave radiations for the synthesis of magnetite (Fe_3O_4) and hematite (α-Fe_2O_3), and used $FeCl_3$, polyethylene glycol, and $N_2H_4.H_2O$ as precursors, finding that the amount of $N_2H_4.H_2O$ has a key role in controlling the final phase of Fe_3O_4 [197].

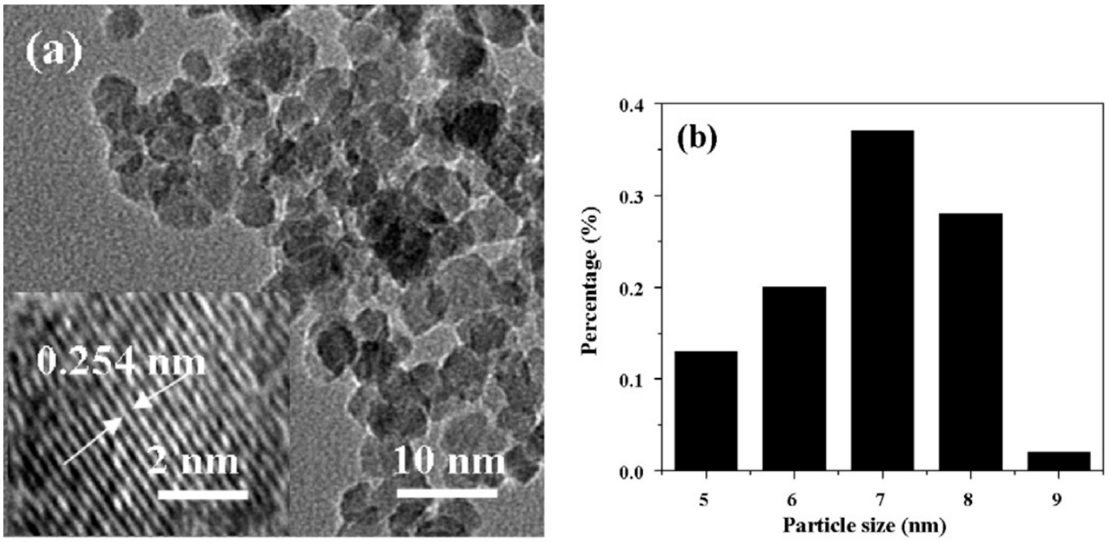

Figure 19. (**a**) TEM image of the $MnFe_2O_4$ and (**b**) the histogram showing particle size (reproduced with permission from Springer 2007) [197].

8.4. Template Assisted Fabrication

Another fabrication method used for the synthesis of MNPs is the template-assisted fabrication [198]. The active template-based synthesis involves the growth of the nuclei at the holes and defects of the template. Subsequently, the growth of the nuclei at the pre-formed template yields the desired morphology of the nanostructures. So through proper selection of base template, the size and shape of the MNPs can be controlled. This technique has two important advantages over the chemical routes:

(i) Template use in the fabrication process determines the final size and morphology of the nanostructures.
(ii) Complex nanostructures such as nanobarcodes (segmented nanorods) nanoprism, nanocubes hexagons, and octahedrons MNPs can be fabricated in an easy manner, with full control on size and morphology.

However, this method has also some drawback. It is a multistep process, first requiring the fabrication base templates and then the subsequent deposition of magnetic material within the template. In the following discussion, we will highlight important recent progress that has been done in the template-assisted synthesis of complex magnetic nanostructures. Mirkin et al. have demonstrated the synthesis of nanobarcodes (segmented nanowires with excellent control of composition along the length) of metals and polymers magnetic and non-magnetic materials. They demonstrated the fabrication of two component rod structure that was made by deposition of hydrophilic Au block and hydrophobic Polypyrrole block on anodic alumina oxide template. Due to the difference in the diameter of hydrophilic Au and hydrophobic Polypyrrole these sections were assembled in unique and exclusive pseudo-conical shape with three-dimensional bundle- and tubular-shaped structure as shown in Figure 20 [199].

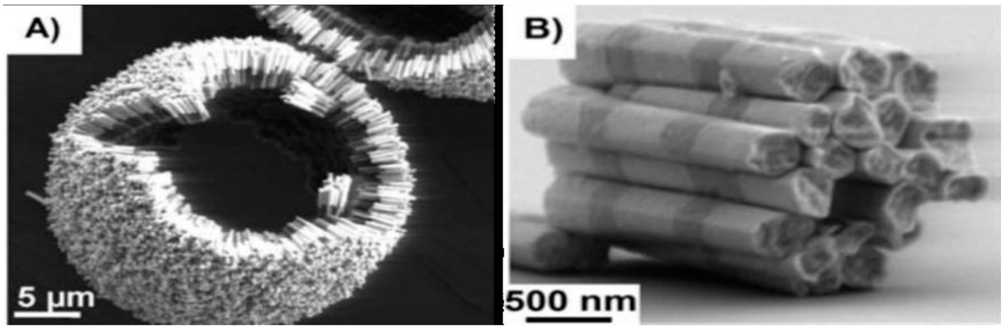

Figure 20. (**A**) SEM image of self-assembly of Au-Polypyrrole rods into a tubular shape. (**B**) SEM image showing the alignment of the ferromagnetic portion in a bundle of Au–Ni rods (reproduced with permission from Wiley Online Library 2006) [199].

8.5. Sol–Gel Method

The sol–gel process is a versatile chemical approach for the synthesis of nanoparticles with precise shapes and size. Sol–gel synthetic strategy makes use of a gelling agent to form a homogeneous gel where a metal salt is stirred [200]. This process involves the hydroxylation and condensation of metal precursors in solution to form a colloid. Sol–gel method provides a wide range of synthesis temperature, for instance, we managed to obtain nearly monodispersed α-Fe_2O_3, γ-Fe_2O_3 and Fe_3O_4 with same procedure and same starting reagent through a medium temperature sol–gel route [201]. Uniquely, the formation of different final iron oxide structures is only dependent on the drying process (Figure 21). The size displayed by TEM revealed that 4.9 nm of Fe_3O_4 nanoparticles are obtained by the centrifugation of sol, whereas slight increment in size of γ-Fe_2O_3 was formed when xerogel was heated at 150 °C. Yet, directly drying of wet Fe_3O_4 gel at 150 °C without the formation of xerogel first allowed phase transformation to 10.1 nm α-Fe_2O_3 [201].

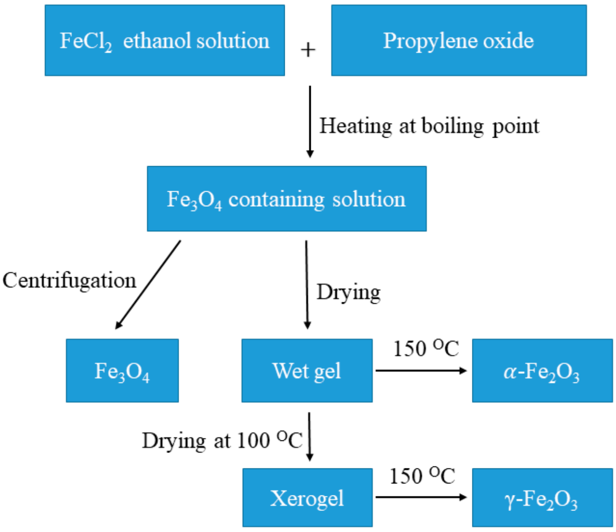

Figure 21. Scheme flow for the preparation of α-Fe_2O_3, γ-Fe_2O_3 and Fe_3O_4 nanoparticles (reproduced with permission from Science Direct 2013) [201].

The sizes of obtained magnetite nanoparticles are readily tailored by longer annealing temperature range under vacuum environment. The magnetic behavior, particle size and crystallinity of magnetite nanoparticles is very sensitive to the annealing temperature where these physico-chemical properties increase as annealing temperature was adjusted from 200 °C to 400 °C [202]. Combination of microwave heating with this route provides a fast and energy efficient synthesis methodology to metal oxide nanoparticles [203]. The reaction mixture of Fe(acec)$_3$ that dissolved in benzyl alcohol was heated at 170 °C by exposure to microwave radiation for 12 min and accomplished to yield 5–6 nm of nanoparticles [204].

8.6. Synthesis of GO-Fe$_3$O$_4$ Nanocomposite

8.6.1. Coprecipitation Method

Graphene oxide was synthesized by well-known Hummers method [205]. To synthesize the GO-Fe$_3$O$_4$ composite, a weighed amount of as-synthesized graphene oxide, prepared by Hummers method, was dispersed in distilled water by sonication. An aqueous solution containing FeCl$_3$ and FeCl$_2$.4H$_2$O was then added into the graphene oxide dispersion kept under constant stirring. After 2 h of stirring, CH$_3$NH$_2$ was added drop wise into the dispersion to precipitate Fe$_3$O$_4$ nanoparticles [206].

8.6.2. Organometallic Decomposition and Ligand Exchange Method

Ferrite nanoparticles with high saturation magnetization, narrow size distribution, and better shape control is achieved by organometallic decomposition method. Nanoparticles synthesized by organometallic decomposition method are not dispersible in water and they are functionalized with biocompatible molecules for further use. GO–nanoparticle composites were synthesized using emulsification process, the details of which are described in Figure 22. The particles are coated with GO and PEG which improves water dispersibility and biocompatibility of PEG-coated particles is well recorded.

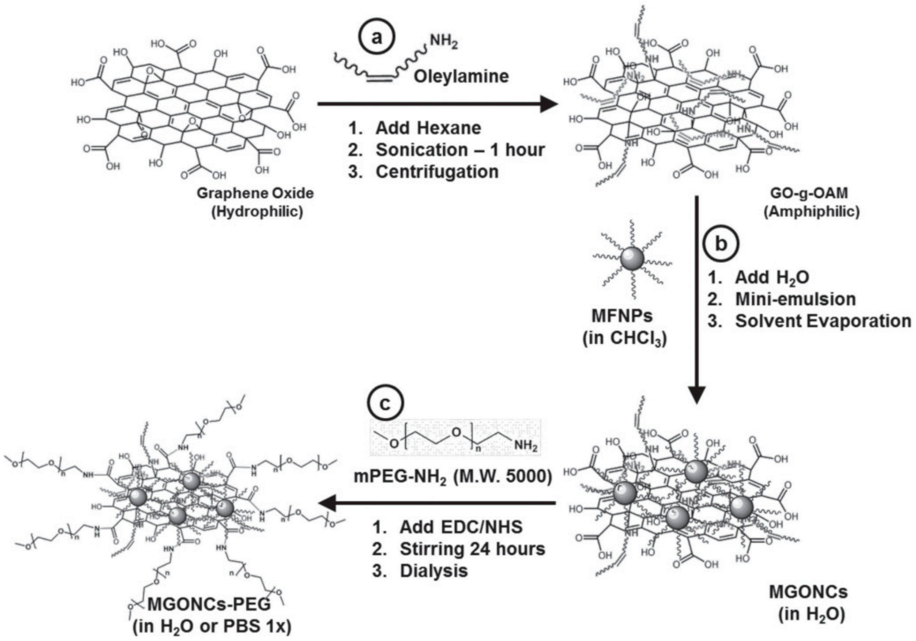

Figure 22. Schematic illustration of the formation of (**a**) amphiphilic graphene oxide sheets (GO-g-OAM), (**b**) water-dispersible NP/GO nanocomposite (MGONC), and (**c**) PEGylation of MGONC (reproduced with permission from Wiley Online Library 2012) [105].

8.7. Cytotoxicity of Ferrite Nanoparticles

The cytotoxicity of the ferrite nanoparticles is thoroughly studied and there are numerous reports of cytotoxicity of ferrite nanoparticles functionalized with various polymeric coatings [207,208]. Ferrite nanoparticles are usually functionalized with chitosan, polyethylene glycol, and graphene oxide [209].

Iron oxide NPs coated with different substances have shown variable cell viability results [210]. There are various in vitro methods, and the LDH, MTT and MTS assays are most widely used for assessment of nanoparticles cytotoxicity [211]. Magnetic iron oxide NPs have been observed to accumulate in the liver, spleen, lungs, and brain after inhalation, showing its ability to cross the blood–brain barrier [212].

9. Conclusions

MH is a cancer therapy method which involves delivering MNPs to the tumor cells and heating them by applying AMF. The world is witnessing great progress in understanding the principles and applications of this noninvasive and localized therapy technique. In this report, we discussed the basic principles of MH using MNPs. The basics of heat generation under an AMF were discussed. Some of the extrinsic and intrinsic parameters that influence heat generation by MNPs were explained. Calorimetric measurements were introduced along with the sources of errors. Several synthesis methods of MNPs where presented. The interesting features of multifunctional hybrid MNPs were also introduced.

Author Contributions: All authors I.M.O., V.N., S.A., S.S. and C.V.V.M.G. contributed equally in the preparation of this review article, including writing—original draft preparation and writing—review and editing.

Funding: This work was financially supported by the UAEU Program for Advanced Research (UPAR) under the Grant no. 31S312.

Conflicts of Interest: The authors declare no conflicts of interest.

References

1. Dou, Y.; Hynynen, K.; Allen, C. To heat or not to heat: Challenges with clinical translation of thermosensitive liposomes. *J. Control Release* **2017**, *249*, 63–73. [CrossRef] [PubMed]
2. Mallory, M.; Gogineni, E.; Jones, G.C.; Greer, L.; Simone, C.B. Therapeutic hyperthermia: The old, the new, and the upcoming. *Crit. Rev. Oncol. Hematol.* **2016**, *97*, 56–64. [CrossRef] [PubMed]
3. Fratila, R.; Fuente, J. *Nanomaterials for Magnetic and Optical Hyperthermia Applications*, 1st ed.; Elsevier: Amsterdam, The Nederland, 2019; pp. 1–10. ISBN 978-0-12-813928-8.
4. Pérez-Hernández, M. Chapter 8—Mechanisms of Cell Death Induced by Optical Hyperthermia. In *Nanomaterials for Magnetic and Optical Hyperthermia Applications*; Micro and Nano Technologies; Fratila, R.M., De La Fuente, J.M., Eds.; Elsevier: Amsterdam, The Netherlands, 2019; pp. 201–228. ISBN 978-0-12-813928-8.
5. Dhavalikar, R.; Bohórquez, A.C.; Rinaldi, C. Chapter 10—Image-Guided Thermal Therapy Using Magnetic Particle Imaging and Magnetic Fluid Hyperthermia. In *Nanomaterials for Magnetic and Optical Hyperthermia Applications*; Micro and Nano Technologies; Fratila, R.M., De La Fuente, J.M., Eds.; Elsevier: Amsterdam, The Netherlands, 2019; pp. 265–286. ISBN 978-0-12-813928-8.
6. Beik, J.; Abed, Z.; Ghoreishi, F.S.; Hosseini-Nami, S.; Mehrzadi, S.; Shakeri-Zadeh, A.; Kamrava, S.K. Nanotechnology in hyperthermia cancer therapy: From fundamental principles to advanced applications. *J. Control Release* **2016**, *235*, 205–221. [CrossRef] [PubMed]
7. Ito, M.; Hiramatsu, H.; Kobayashi, K.; Suzue, K.; Kawahata, M.; Hioki, K.; Ueyama, Y.; Koyanagi, Y.; Sugamura, K.; Tsuji, K.; et al. NOD/SCID/gamma(c)(null) mouse: An excellent recipient mouse model for engraftment of human cells. *Blood* **2002**, *100*, 3175–3182. [CrossRef]
8. Di Corato, R.; Espinosa, A.; Lartigue, L.; Tharaud, M.; Chat, S.; Pellegrino, T.; Ménager, C.; Gazeau, F.; Wilhelm, C. Magnetic hyperthermia efficiency in the cellular environment for different nanoparticle designs. *Biomaterials* **2014**, *35*, 6400–6411. [CrossRef]
9. Fratila, R.M.; Fuente, J.M.D.L. *Nanomaterials for Magnetic and Optical Hyperthermia Applications*; Elsevier: Amsterdam, The Netherlands, 2018; ISBN 978-0-12-813929-5.
10. Laurent, S.; Dutz, S.; Häfeli, U.O.; Mahmoudi, M. Magnetic fluid hyperthermia: Focus on superparamagnetic iron oxide nanoparticles. *Adv. Colloid Interface Sci.* **2011**, *166*, 8–23. [CrossRef]
11. Kumar, C.S.S.R.; Mohammad, F. Magnetic nanomaterials for hyperthermia-based therapy and controlled drug delivery. *Adv. Drug Deliv. Rev.* **2011**, *63*, 789–808. [CrossRef]

12. Hergt, R.; Dutz, S.; Müller, R.; Zeisberger, M. Magnetic particle hyperthermia: Nanoparticle magnetism and materials development for cancer therapy. *J. Phys. Condens. Matter* **2006**, *18*, S2919–S2934. [CrossRef]
13. Vallejo-Fernandez, G.; Whear, O.; Roca, A.G.; Hussain, S.; Timmis, J.; Patel, V.; Grady, K. Mechanisms of hyperthermia in magnetic nanoparticles. *J. Phys. D Appl. Phys.* **2013**, *46*, 312001. [CrossRef]
14. Piñeiro, Y.; Vargas, Z.; Rivas, J.; López-Quintela, M.A. Iron Oxide Based Nanoparticles for Magnetic Hyperthermia Strategies in Biological Applications. *Eur. J. Inorganic Chem.* **2015**, *2015*, 4495–4509.
15. Dennis, C.L.; Ivkov, R. Physics of heat generation using magnetic nanoparticles for hyperthermia. *Int. J. Hyperth.* **2013**, *29*, 715–729. [CrossRef] [PubMed]
16. Obaidat, I.M.; Issa, B.; Haik, Y. Magnetic Properties of Magnetic Nanoparticles for Efficient Hyperthermia. *Nanomaterials* **2015**, *5*, 63–89. [CrossRef] [PubMed]
17. Périgo, E.A.; Hemery, G.; Sandre, O.; Ortega, D.; Garaio, E.; Plazaola, F.; Teran, F.J. Fundamentals and advances in magnetic hyperthermia. *Appl. Phys. Rev.* **2015**, *2*, 041302. [CrossRef]
18. Mahmoudi, K.; Bouras, A.; Bozec, D.; Ivkov, R.; Hadjipanayis, C. Magnetic hyperthermia therapy for the treatment of glioblastoma: A review of the therapy's history, efficacy and application in humans. *Int. J. Hyperth.* **2018**, *34*, 1316–1328. [CrossRef]
19. Angelakeris, M. Magnetic nanoparticles: A multifunctional vehicle for modern theranostics. *Biochim. Biophys. Acta Gen. Subj.* **2017**, *1861*, 1642–1651. [CrossRef]
20. Spirou, S.V.; Costa Lima, S.A.; Bouziotis, P.; Vranješ-Djurić, S.; Efthimiadou, E.K.; Laurenzana, A.; Barbosa, A.I.; Garcia-Alonso, I.; Jones, C.; Jankovic, D.; et al. Recommendations for in Vitro and In Vivo Testing of Magnetic Nanoparticle Hyperthermia Combined with Radiation Therapy. *Nanomaterials* **2018**, *8*, 306. [CrossRef]
21. Spirou, S.V.; Basini, M.; Lascialfari, A.; Sangregorio, C.; Innocenti, C. Magnetic Hyperthermia and Radiation Therapy: Radiobiological Principles and Current Practice. *Nanomaterials* **2018**, *8*, 401. [CrossRef]
22. Issa, B.; Obaidat, I.M.; Albiss, B.A.; Haik, Y. Magnetic nanoparticles: Surface effects and properties related to biomedicine applications. *Int. J. Mol. Sci.* **2013**, *14*, 21266–21305. [CrossRef]
23. Carrey, J.; Mehdaoui, B.; Respaud, M. Simple models for dynamic hysteresis loop calculations of magnetic single-domain nanoparticles: Application to magnetic hyperthermia optimization. *J. Appl. Phys.* **2011**, *109*, 083921. [CrossRef]
24. Mehdaoui, B.; Meffre, A.; Carrey, J.; Lachaize, S.; Lacroix, L.-M.; Gougeon, M.; Chaudret, B.; Respaud, M. Optimal Size of Nanoparticles for Magnetic Hyperthermia: A Combined Theoretical and Experimental Study. *Adv. Funct. Mater.* **2011**, *21*, 4573–4581. [CrossRef]
25. Colombo, M.; Carregal-Romero, S.; Casula, M.F.; Gutiérrez, L.; Morales, M.P.; Boehm, I.; Heverhagen, J.T.; Prosperi, D.; Parak, W.J. Biological applications of magnetic nanoparticles. *Chem. Soc. Rev.* **2012**, *41*, 4306–4334. [CrossRef] [PubMed]
26. Obaidat, I.M.; Nayek, C.; Manna, K.; Bhattacharjee, G.; Al-Omari, I.A.; Gismelseed, A. Investigating Exchange Bias and Coercivity in Fe_3O_4–γ-Fe_2O_3 Core–Shell Nanoparticles of Fixed Core Diameter and Variable Shell Thicknesses. *Nanomaterials* **2017**, *7*, 415. [CrossRef] [PubMed]
27. Obaidat, I.M.; Nayek, C.; Manna, K. Investigating the Role of Shell Thickness and Field Cooling on Saturation Magnetization and Its Temperature Dependence in $Fe3O_4$/γ-Fe_2O_3 Core/Shell Nanoparticles. *Appl. Sci.* **2017**, *7*, 1269. [CrossRef]
28. Rachakatla, R.S.; Balivada, S.; Seo, G.-M.; Myers, C.B.; Wang, H.; Samarakoon, T.N.; Dani, R.; Pyle, M.; Kroh, F.O.; Walker, B.; et al. Attenuation of mouse melanoma by A/C magnetic field after delivery of bi-magnetic nanoparticles by neural progenitor cells. *ACS Nano* **2010**, *4*, 7093–7104. [CrossRef]
29. Ruiz, A.; Gutiérrez, L.; Cáceres-Vélez, P.R.; Santos, D.; Chaves, S.B.; Fascineli, M.L.; Garcia, M.P.; Azevedo, R.B.; Morales, M.P. Biotransformation of magnetic nanoparticles as a function of coating in a rat model. *Nanoscale* **2015**, *7*, 16321–16329. [CrossRef]
30. Guimarães, A.P. The Basis of Nanomagnetism. In *Principles of Nanomagnetism*; NanoScience and Technology; Guimarães, A.P., Ed.; Springer International Publishing: Cham, Switzerland, 2017; pp. 1–23, ISBN 978-3-319-59409-5.
31. Deatsch, A.E.; Evans, B.A. Heating efficiency in magnetic nanoparticle hyperthermia. *J. Magn. Magn. Mater.* **2014**, *354*, 163–172. [CrossRef]
32. Brown, W.F. Thermal Fluctuations of a Single-Domain Particle. *Phys. Rev.* **1963**, *130*, 1677–1686. [CrossRef]
33. Néel, L. Théorie du traînage magnétique des substances massives dans le domaine de Rayleigh. *J. Phys. Radium* **1950**, *11*, 49–61. [CrossRef]

34. Leslie-Pelecky, D.L.; Rieke, R.D. Magnetic Properties of Nanostructured Materials. *Chem. Mater.* **1996**, *8*, 1770–1783. [CrossRef]
35. Rosensweig, R.E. Heating magnetic fluid with alternating magnetic field. *J. Magn. Magn. Mater.* **2002**, *252*, 370–374. [CrossRef]
36. Delaunay, L.; Neveu, S.; Noyel, G.; Monin, J. A new spectrometric method, using a magneto-optical effect, to study magnetic liquids. *J. Magn. Magn. Mater.* **1995**, *149*, L239–L245. [CrossRef]
37. Glöckl, G.; Hergt, R.; Zeisberger, M.; Dutz, S.; Nagel, S.; Weitschies, W. The effect of field parameters, nanoparticle properties and immobilization on the specific heating power in magnetic particle hyperthermia. *J. Phys. Condens. Matter* **2006**, *18*, S2935–S2949. [CrossRef]
38. Hergt, R.; Dutz, S. Magnetic particle hyperthermia—Biophysical limitations of a visionary tumour therapy. *J. Magn. Magn. Mater.* **2007**, *311*, 187–192. [CrossRef]
39. Moroz, P.; Jones, S.K.; Gray, B.N. Magnetically mediated hyperthermia: Current status and future directions. *Int. J. Hyperth.* **2002**, *18*, 267–284. [CrossRef]
40. Fantechi, E.; Innocenti, C.; Albino, M.; Lottini, E.; Sangregorio, C. Influence of cobalt doping on the hyperthermic efficiency of magnetite nanoparticles. *J. Magn. Magn. Mater.* **2015**, *380*, 365–371. [CrossRef]
41. Lee, J.-H.; Jang, J.-T.; Choi, J.-S.; Moon, S.H.; Noh, S.-H.; Kim, J.-W.; Kim, J.-G.; Kim, I.-S.; Park, K.I.; Cheon, J. Exchange-coupled magnetic nanoparticles for efficient heat induction. *Nat. Nanotechnol.* **2011**, *6*, 418–422. [CrossRef]
42. Obaidat, I.M.; Mohite, V.; Issa, B.; Tit, N.; Haik, Y. Predicting a major role of surface spins in the magnetic properties of ferrite nanoparticles. *Cryst. Res. Technol.* **2009**, *44*, 489–494. [CrossRef]
43. Cotin, G.; Perton, F.; Blanco-Andujar, C.; Pichon, B.; Mertz, D.; Bégin-Colin, S. Chapter 2—Design of Anisotropic Iron-Oxide-Based Nanoparticles for Magnetic Hyperthermia. In *Nanomaterials for Magnetic and Optical Hyperthermia Applications*; Micro and Nano Technologies; Fratila, R.M., De La Fuente, J.M., Eds.; Elsevier: Amsterdam, The Netherlands, 2019; pp. 41–60. ISBN 978-0-12-813928-8.
44. Cullity, B.D.; Graham, C.D. *Introduction to Magnetic Materials*; Wiley: Hoboken IEEE Press: Chichester, UK, 2009; ISBN 978-0-471-47741-9.
45. Guardia, P.; Di Corato, R.; Lartigue, L.; Wilhelm, C.; Espinosa, A.; Garcia-Hernandez, M.; Gazeau, F.; Manna, L.; Pellegrino, T. Water-Soluble Iron Oxide Nanocubes with High Values of Specific Absorption Rate for Cancer Cell Hyperthermia Treatment. *ACS Nano* **2012**, *6*, 3080–3091. [CrossRef]
46. Martinez-Boubeta, C.; Simeonidis, K.; Makridis, A.; Angelakeris, M.; Iglesias, O.; Guardia, P.; Cabot, A.; Yedra, L.; Estrade, S.; Peiro, F.; et al. Learning from Nature to Improve the Heat Generation of Iron-Oxide Nanoparticles for Magnetic Hyperthermia Applications. *Sci. Rep.* **2013**. [CrossRef]
47. Usov, N.A.; Nesmeyanov, M.S.; Gubanova, E.M.; Epshtein, N.B. Heating ability of magnetic nanoparticles with cubic and combined anisotropy. *Beilstein J. Nanotechnol.* **2019**, *10*, 305–314. [CrossRef]
48. Nayek, C.; Manna, K.; Bhattacharjee, G.; Murugavel, P.; Obaidat, I. Investigating Size- and Temperature-Dependent Coercivity and Saturation Magnetization in PEG Coated Fe_3O_4 Nanoparticles. *Magnetochemistry* **2017**, *3*, 19. [CrossRef]
49. Liu, W.; Zhong, W.; Du, Y.W. Magnetic nanoparticles with core/shell structures. *J. NanoSci. Nanotechnol.* **2008**, *8*, 2781–2792. [CrossRef] [PubMed]
50. Venkatesha, N.; Qurishi, Y.; Atreya, H.S.; Srivastava, C. Effect of core–shell nanoparticle geometry on the enhancement of the proton relaxivity value in a nuclear magnetic resonance experiment. *RSC Adv.* **2016**, *6*, 64605–64610. [CrossRef]
51. Obaidat, I.M.; Haik, Y.; Mohite, V.; Issa, B.; Tit, N. Peculiar Magnetic Properties of MnZnGdFeO Nanoparticles. *Adv. Sci. Lett.* **2009**, *2*, 60–64. [CrossRef]
52. Venkatesha, N.; Pudakalakatti, S.M.; Qurishi, Y.; Atreya, H.S.; Srivastava, C. $MnFe_2O_4$–Fe_3O_4 core–shell nanoparticles as a potential contrast agent for magnetic resonance imaging. *RSC Adv.* **2015**, *5*, 97807–97815. [CrossRef]
53. Mandal, S.; Chaudhuri, K. Engineered magnetic core shell nanoprobes: Synthesis and applications to cancer imaging and therapeutics. *World J. Biol. Chem.* **2016**, *7*, 158–167. [CrossRef] [PubMed]
54. Sun, X.; Huls, N.F.; Sigdel, A.; Sun, S. Tuning exchange bias in core/shell FeO/Fe_3O_4 nanoparticles. *Nano Lett.* **2012**, *12*, 246–251. [CrossRef]

55. Nayek, C.; Al-Akhras, M.-A.; Narayanaswamy, V.; Khaleel, A.; Al-Omari, I.A.; Rusydi, A.; Obaidat, I.M. Role of Shell Thickness and Applied Field on The Magnetic Anisotropy and Temperature Dependence of Coercivity in Fe_3O_4 -Fe_2O_3 Core/shell Nanoparticles. *Mater. Express* **2019**, *9*, 2158–5849. [CrossRef]
56. Thomas, S.; Reethu, K.; Thanveer, T.; Myint, M.T.Z.; Al-Harthi, S.H. Effect of shell thickness on the exchange bias blocking temperature and coercivity in Co-CoO core-shell nanoparticles. *J. Appl. Phys.* **2017**, *122*, 063902. [CrossRef]
57. Dimitriadis, V.; Kechrakos, D.; Chubykalo-Fesenko, O.; Tsiantos, V. Shape-dependent exchange bias effect in magnetic nanoparticles with core-shell morphology. *Phys. Rev. B* **2015**, *92*, 064420. [CrossRef]
58. Nogués, J.; Sort, J.; Langlais, V.; Skumryev, V.; Suriñach, S.; Muñoz, J.S.; Baró, M.D. Exchange bias in nanostructures. *Phys. Rep.* **2005**, *422*, 65–117. [CrossRef]
59. López-Ortega, A.; Estrader, M.; Salazar-Alvarez, G.; Roca, A.G.; Nogués, J. Applications of exchange coupled bi-magnetic hard/soft and soft/hard magnetic core/shell nanoparticles. *Phys. Rep.* **2015**, *553*, 1–32. [CrossRef]
60. Phan, M.-H.; Alonso, J.; Khurshid, H.; Lampen-Kelley, P.; Chandra, S.; Stojak Repa, K.; Nemati, Z.; Das, R.; Iglesias, Ó.; Srikanth, H. Exchange Bias Effects in Iron Oxide-Based Nanoparticle Systems. *Nanomaterials* **2016**, *6*, 221. [CrossRef] [PubMed]
61. Desautels, R.D.; Skoropata, E.; Chen, Y.-Y.; Ouyang, H.; Freeland, J.W.; van Lierop, J. Tuning the surface magnetism of γ-Fe2O3 nanoparticles with a Cu shell. *Appl. Phys. Lett.* **2011**, *99*, 262501. [CrossRef]
62. Rostamnejadi, A.; Venkatesan, M.; Alaria, J.; Boese, M.; Kameli, P.; Salamati, H.; Coey, J.M.D. Conventional and inverse magnetocaloric effects in La0.45Sr0.55MnO_3 nanoparticles. *J. Appl. Phys.* **2011**, *110*, 043905. [CrossRef]
63. Batlle, X.; Labarta, A. Finite-size effects in fine particles: Magnetic and transport properties. *J. Phys. D Appl. Phys.* **2002**. [CrossRef]
64. Ho, C.-H.; Lai, C.-H. Size-Dependent Magnetic Properties of PtMn Nanoparticles. *IEEE Trans. Magn.* **2006**, *42*, 3069–3071. [CrossRef]
65. Zhao, Q.; Wang, L.; Cheng, R.; Mao, L.; Arnold, R.D.; Howerth, E.W.; Chen, Z.G.; Platt, S. Magnetic Nanoparticle-Based Hyperthermia for Head & Neck Cancer in Mouse Models. *Theranostics* **2012**, *2*, 113–121.
66. Nieskoski, M.D.; Trembly, B.S. Comparison of a single optimized coil and a Helmholtz pair for magnetic nanoparticle hyperthermia. *IEEE Trans. Biomed. Eng.* **2014**, *61*, 1642–1650. [CrossRef]
67. Cabrera, D.; Rubia-Rodríguez, I.; Garaio, E.; Plazaola, F.; Dupré, L.; Farrow, N.; Terán, F.J.; Ortega, D. Chapter 5—Instrumentation for Magnetic Hyperthermia. In *Nanomaterials for Magnetic and Optical Hyperthermia Applications*; Micro and Nano Technologies; Fratila, R.M., De La Fuente, J.M., Eds.; Elsevier: Amsterdam, The Netherlands, 2019; pp. 111–138. ISBN 978-0-12-813928-8.
68. Mamiya, H.; Jeyadevan, B. Chapter 1—Design Criteria of Thermal Seeds for Magnetic Fluid Hyperthermia—From Magnetic Physics Point of View. In *Nanomaterials for Magnetic and Optical Hyperthermia Applications*; Micro and Nano Technologies; Fratila, R.M., De La Fuente, J.M., Eds.; Elsevier: Amsterdam, The Netherlands, 2019; pp. 13–39. ISBN 978-0-12-813928-8.
69. Hergt, R.; Hiergeist, R.; Hilger, I.; Kaiser, W.A.; Boguslavsky, Y.; Margel, S.; Richter, U. Maghemite nanoparticles with very high AC-losses for application in RF-magnetic hyperthermia. *J. Magn. Magn. Mater.* **2004**, *270*, 345–357. [CrossRef]
70. Dössel, O.; Bohnert, J. Safety considerations for magnetic fields of 10 mT to 100 mT amplitude in the frequency range of 10 kHz to 100 kHz for magnetic particle imaging. *Biomed. Tech. (Berl)* **2013**, *58*, 611–621. [CrossRef] [PubMed]
71. Kita, E.; Oda, T.; Kayano, T.; Sato, S.; Minagawa, M.; Yanagihara, H.; Kishimoto, M.; Mitsumata, C.; Hashimoto, S.; Yamada, K.; et al. Ferromagnetic nanoparticles for magnetic hyperthermia and thermoablation therapy. *J. Phys. D Appl. Phys.* **2010**, *43*, 474011. [CrossRef]
72. Lemal, P.; Balog, S.; Geers, C.; Taladriz-Blanco, P.; Palumbo, A.; Hirt, A.M.; Rothen-Rutishauser, B.; Petri-Fink, A. Heating behavior of magnetic iron oxide nanoparticles at clinically relevant concentration. *J. Magn. Magn. Mater.* **2019**, *474*, 637–642. [CrossRef]
73. Ovejero, J.G.; Cabrera, D.; Carrey, J.; Valdivielso, T.; Salas, G.; Teran, F.J. Effects of inter- and intra-aggregate magnetic dipolar interactions on the magnetic heating efficiency of iron oxide nanoparticles. *Phys. Chem. Chem. Phys.* **2016**, *18*, 10954–10963. [CrossRef]

74. Narayanaswamy, V.; Obaidat, I.M.; Latiyan, S.; Jain, S.; Nayek, C.; Goankar, S.; AL-Akhras, M.-A.; Al-Omari, I.A. Role of interface quality in iron oxide core/shell nanoparticles on heating efficiency and transverse relaxivity. *Mater. Express* **2019**, 2158–5849. [CrossRef]
75. Narayanaswamy, V.; Obaidat, I.M.; Kamzin, A.S.; Latiyan, S.; Jain, S.; Kumar, H.; Srivastava, C.; Alaabed, S.; Issa, B. Synthesis of Graphene Oxide-Fe_3O_4 Based Nanocomposites Using the Mechanochemical Method and in Vitro Magnetic Hyperthermia. *Int. J. Mol. Sci.* **2019**, *20*, 3368. [CrossRef]
76. Espinosa, A.; Di Corato, R.; Kolosnjaj-Tabi, J.; Flaud, P.; Pellegrino, T.; Wilhelm, C. Duality of Iron Oxide Nanoparticles in Cancer Therapy: Amplification of Heating Efficiency by Magnetic Hyperthermia and Photothermal Bimodal Treatment. *ACS Nano* **2016**, *10*, 2436–2446. [CrossRef]
77. Kandasamy, G.; Sudame, A.; Bhati, P.; Chakrabarty, A.; Maity, D. Systematic investigations on heating effects of carboxyl-amine functionalized superparamagnetic iron oxide nanoparticles (SPIONs) based ferrofluids for in vitro cancer hyperthermia therapy. *J. Mol. Liq.* **2018**, *256*, 224–237. [CrossRef]
78. de la Presa, P.; Luengo, Y.; Velasco, V.; Morales, M.P.; Iglesias, M.; Veintemillas-Verdaguer, S.; Crespo, P.; Hernando, A. Particle Interactions in Liquid Magnetic Colloids by Zero Field Cooled Measurements: Effects on Heating Efficiency. *J. Phys. Chem. C* **2015**, *119*, 11022–11030. [CrossRef]
79. Blanco-Andujar, C.; Ortega, D.; Southern, P.; Nesbitt, S.A.; Thanh, N.T.K.; Pankhurst, Q.A. Real-time tracking of delayed-onset cellular apoptosis induced by intracellular magnetic hyperthermia. *Nanomedicine (Lond)* **2016**, *11*, 121–136. [CrossRef]
80. Wan, J.; Yuan, R.; Zhang, C.; Wu, N.; Yan, F.; Yu, S.; Chen, K. Stable and Biocompatible Colloidal Dispersions of Superparamagnetic Iron Oxide Nanoparticles with Minimum Aggregation for Biomedical Applications. *J. Phys. Chem. C* **2016**, *120*, 23799–23806. [CrossRef]
81. Shetake, N.G.; Kumar, A.; Gaikwad, S.; Ray, P.; Desai, S.; Ningthoujam, R.S.; Vatsa, R.K.; Pandey, B.N. Magnetic nanoparticle-mediated hyperthermia therapy induces tumour growth inhibition by apoptosis and Hsp90/AKT modulation. *Int. J. Hyperth.* **2015**, *31*, 909–919. [CrossRef] [PubMed]
82. Sakellari, D.; Brintakis, K.; Kostopoulou, A.; Myrovali, E.; Simeonidis, K.; Lappas, A.; Angelakeris, M. Ferrimagnetic nanocrystal assemblies as versatile magnetic particle hyperthermia mediators. *Mater. Sci. Eng. C Mater. Biol. Appl.* **2016**, *58*, 187–193. [CrossRef] [PubMed]
83. Mendo, S.G.; Alves, A.F.; Ferreira, L.P.; Cruz, M.M.; Mendonça, M.H.; Godinho, M.; Carvalho, M.D. Hyperthermia studies of ferrite nanoparticles synthesized in the presence of cotton. *New J. Chem.* **2015**, *39*, 7182–7193. [CrossRef]
84. Burrows, F.; Parker, C.; Evans, R.F.L.; Hancock, Y.; Hovorka, O.; Chantrell, R.W. Energy losses in interacting fine-particle magnetic composites. *J. Phys. D Appl. Phys.* **2010**, *43*, 474010. [CrossRef]
85. Tan, R.P.; Carrey, J.; Respaud, M. Magnetic hyperthermia properties of nanoparticles inside lysosomes using kinetic Monte Carlo simulations: Influence of key parameters and dipolar interactions, and evidence for strong spatial variation of heating power. *Phys. Rev. B* **2014**, *90*, 214421. [CrossRef]
86. Coral, D.F.; Mendoza Zélis, P.; Marciello, M.; Morales, M.d.P.; Craievich, A.; Sánchez, F.H.; Fernández van Raap, M.B. Effect of Nanoclustering and Dipolar Interactions in Heat Generation for Magnetic Hyperthermia. *Langmuir* **2016**, *32*, 1201–1213. [CrossRef]
87. Mamiya, H. Recent Advances in Understanding Magnetic Nanoparticles in AC Magnetic Fields and Optimal Design for Targeted Hyperthermia. Available online: https://www.hindawi.com/journals/jnm/2013/752973/ (accessed on 10 October 2019).
88. Mamiya, H.; Jeyadevan, B. Hyperthermic effects of dissipative structures of magnetic nanoparticles in large alternating magnetic fields. *Sci. Rep.* **2011**, *1*, 157. [CrossRef]
89. Usov, N.A. Low frequency hysteresis loops of superparamagnetic nanoparticles with uniaxial anisotropy. *J. Appl. Phys.* **2010**, *107*, 123909. [CrossRef]
90. Raikher, Y.L.; Stepanov, V.I. Physical aspects of magnetic hyperthermia: Low-frequency ac field absorption in a magnetic colloid. *J. Magne. Magn. Mater.* **2014**, *368*, 421–427. [CrossRef]
91. Raikher, Y.; Stepanov, V. Absorption of AC field energy in a suspension of magnetic dipoles. *J. Magn. Magn. Mater.* **2008**, *320*, 2692–2695. [CrossRef]
92. Andreu, I.; Natividad, E. Accuracy of available methods for quantifying the heat power generation of nanoparticles for magnetic hyperthermia. *Int. J. Hyperth.* **2013**, *29*, 739–751. [CrossRef]

93. Drayton, A.; Zehner, J.; Timmis, J.; Patel, V.; Vallejo-Fernandez, G.; O'Grady, K. A comparative measurement technique of nanoparticle heating for magnetic hyperthermia applications. *J. Phys. D Appl. Phys.* **2017**, *50*, 495003. [CrossRef]
94. Wildeboer, R.R.; Southern, P.; Pankhurst, Q.A. On the reliable measurement of specific absorption rates and intrinsic loss parameters in magnetic hyperthermia materials. *J. Phys. D Appl. Phys.* **2014**, *47*, 495003. [CrossRef]
95. Lemal, P.; Geers, C.; Rothen-Rutishauser, B.; Lattuada, M.; Petri-Fink, A. Measuring the heating power of magnetic nanoparticles: An overview of currently used methods. *Mater. Today Proc.* **2017**, *4*, S107–S117. [CrossRef]
96. Bordelon, D.E.; Cornejo, C.; Grüttner, C.; Westphal, F.; DeWeese, T.L.; Ivkov, R. Magnetic nanoparticle heating efficiency reveals magneto-structural differences when characterized with wide ranging and high amplitude alternating magnetic fields. *J. Appl. Phys.* **2011**, *109*, 124904. [CrossRef]
97. Verde, E.L.; Landi, G.T.; Carrião, M.S.; Drummond, A.L.; Gomes, J.A.; Vieira, E.D.; Sousa, M.H.; Bakuzis, A.F. Field dependent transition to the non-linear regime in magnetic hyperthermia experiments: Comparison between maghemite, copper, zinc, nickel and cobalt ferrite nanoparticles of similar sizes. *Aip Adv.* **2012**, *2*, 032120. [CrossRef]
98. Soetaert, F.; Kandala, S.K.; Bakuzis, A.; Ivkov, R. Experimental estimation and analysis of variance of the measured loss power of magnetic nanoparticles. *Sci. Rep.* **2017**, *7*, 6661. [CrossRef]
99. Natividad, E.; Castro, M.; Mediano, A. Adiabatic vs. non-adiabatic determination of specific absorption rate of ferrofluids. *J. Magn. Magn. Mater.* **2009**, *321*, 1497–1500. [CrossRef]
100. Landi, G.T. Simple models for the heating curve in magnetic hyperthermia experiments. *J. Magn. Magn. Mater.* **2013**, *326*, 14–21. [CrossRef]
101. Wang, S.-Y.; Huang, S.; Borca-Tasciuc, D.-A. Potential Sources of Errors in Measuring and Evaluating the Specific Loss Power of Magnetic Nanoparticles in an Alternating Magnetic Field. *IEEE Trans. Magn.* **2013**, *49*, 255–262. [CrossRef]
102. Lv, Y.; Yang, Y.; Fang, J.; Zhang, H.; Peng, E.; Liu, X.; Xiao, W.; Ding, J. Size dependent magnetic hyperthermia of octahedral Fe3O4 nanoparticles. *RSC Adv.* **2015**, *5*, 76764–76771. [CrossRef]
103. Liu, X.L.; Yang, Y.; Ng, C.T.; Zhao, L.Y.; Zhang, Y.; Bay, B.H.; Fan, H.M.; Ding, J. Magnetic vortex nanorings: A new class of hyperthermia agent for highly efficient in vivo regression of tumors. *Adv. Mater. Weinh.* **2015**, *27*, 1939–1944. [CrossRef] [PubMed]
104. Yang, Y.; Liu, X.; Lv, Y.; Herng, T.S.; Xu, X.; Xia, W.; Zhang, T.; Fang, J.; Xiao, W.; Ding, J. Orientation Mediated Enhancement on Magnetic Hyperthermia of Fe3O4 Nanodisc. *Adv. Funct. Mater.* **2015**, *25*, 812–820. [CrossRef]
105. Peng, E.; Choo, E.S.G.; Chandrasekharan, P.; Yang, C.-T.; Ding, J.; Chuang, K.-H.; Xue, J.M. Synthesis of Manganese Ferrite/Graphene Oxide Nanocomposites for Biomedical Applications. *Small* **2012**, *8*, 3620–3630. [CrossRef]
106. Niculaes, D.; Lak, A.; Anyfantis, G.C.; Marras, S.; Laslett, O.; Avugadda, S.K.; Cassani, M.; Serantes, D.; Hovorka, O.; Chantrell, R.; et al. Asymmetric Assembling of Iron Oxide Nanocubes for Improving Magnetic Hyperthermia Performance. *ACS Nano* **2017**, *11*, 12121–12133. [CrossRef]
107. Sugumaran, P.J.; Liu, X.-L.; Herng, T.S.; Peng, E.; Ding, J. GO-Functionalized Large Magnetic Iron Oxide Nanoparticles with Enhanced Colloidal Stability and Hyperthermia Performance. *ACS Appl. Mater. Interfaces* **2019**, *11*, 22703–22713. [CrossRef]
108. Zhu, M.; Wu, L.; Rao, F.; Song, Z.; Ren, K.; Ji, X.; Song, S.; Yao, D.; Feng, S. Uniform Ti-doped Sb2Te3 materials for high-speed phase change memory applications. *Appl. Phys. Lett.* **2014**, *104*, 053119. [CrossRef]
109. Ortgies, D.H.; de la Cueva, L.; del Rosal, B.; Sanz-Rodríguez, F.; Fernández, N.; Iglesias-de la Cruz, M.C.; Salas, G.; Cabrera, D.; Teran, F.J.; Jaque, D.; et al. In Vivo Deep Tissue Fluorescence and Magnetic Imaging Employing Hybrid Nanostructures. *ACS Appl. Mater. Interfaces* **2016**, *8*, 1406–1414. [CrossRef]
110. Rieke, V.; Pauly, K.B. MR thermometry. *J. Magn. Reson. Imaging* **2008**, *27*, 376–390. [CrossRef]
111. Dhavalikar, R.; Rinaldi, C. Theoretical Predictions for Spatially-Focused Heating of Magnetic Nanoparticles Guided by Magnetic Particle Imaging Field Gradients. *J. Magn. Magn. Mater.* **2016**, *419*, 267–273. [CrossRef] [PubMed]
112. Murase, K.; Takata, H.; Takeuchi, Y.; Saito, S. Control of the temperature rise in magnetic hyperthermia with use of an external static magnetic field. *Phys. Med.* **2013**, *29*, 624–630. [CrossRef] [PubMed]

113. Barati, M.R.; Selomulya, C.; Sandeman, K.G.; Suzuki, K. Extraordinary induction heating effect near the first order Curie transition. *Appl. Phys. Lett.* **2014**, *105*, 162412. [CrossRef]
114. Rauwerdink, A.M.; Hansen, E.W.; Weaver, J.B. Nanoparticle temperature estimation in combined ac and dc magnetic fields. *Phys. Med. Biol.* **2009**, *54*, L51–L55. [CrossRef]
115. Weaver, J.B.; Rauwerdink, A.M.; Hansen, E.W. Magnetic nanoparticle temperature estimation. *Med. Phys.* **2009**, *36*, 1822–1829. [CrossRef]
116. Zhong, J.; Liu, W.; Du, Z.; César de Morais, P.; Xiang, Q.; Xie, Q. A noninvasive, remote and precise method for temperature and concentration estimation using magnetic nanoparticles. *Nanotechnology* **2012**, *23*, 075703. [CrossRef]
117. Akin, Y.; Obaidat, I.M.; Issa, B.; Haik, Y. Ni1-x Crx alloy for self controlled magnetic hyperthermia. *Cryst. Res. Technol.* **2009**, *44*, 386–390. [CrossRef]
118. Zhong, J.; Dieckhoff, J.; Schilling, M.; Ludwig, F. Influence of static magnetic field strength on the temperature resolution of a magnetic nanoparticle thermometer. *J. Appl. Phys.* **2016**, *120*, 143902. [CrossRef]
119. Garaio, E.; Collantes, J.-M.; Garcia, J.A.; Plazaola, F.; Sandre, O. Harmonic phases of the nanoparticle magnetization: An intrinsic temperature probe. *Appl. Phys. Lett.* **2015**, *107*, 123103. [CrossRef]
120. Garaio, E.; Collantes, J.M.; Plazaola, F.; Garcia, J.A.; Castellanos-Rubio, I. A multifrequency eletromagnetic applicator with an integrated AC magnetometer for magnetic hyperthermia experiments. *Meas. Sci. Technol.* **2014**, *25*, 115702. [CrossRef]
121. Connord, V.; Mehdaoui, B.; Tan, R.P.; Carrey, J.; Respaud, M. An air-cooled Litz wire coil for measuring the high frequency hysteresis loops of magnetic samples–a useful setup for magnetic hyperthermia applications. *Rev. Sci. Instrum.* **2014**, *85*, 093904. [CrossRef] [PubMed]
122. Garaio, E.; Sandre, O.; Collantes, J.-M.; Garcia, J.A.; Mornet, S.; Plazaola, F. Specific absorption rate dependence on temperature in magnetic field hyperthermia measured by dynamic hysteresis losses (ac magnetometry). *Nanotechnology* **2015**, *26*, 015704. [CrossRef] [PubMed]
123. Hildebrandt, B.; Wust, P.; Ahlers, O.; Dieing, A.; Sreenivasa, G.; Kerner, T.; Felix, R.; Riess, H. The cellular and molecular basis of hyperthermia. *Crit. Rev. Oncol. Hematol.* **2002**, *43*, 33–56. [CrossRef]
124. Chang, D.; Lim, M.; Goos, J.A.C.M.; Qiao, R.; Ng, Y.Y.; Mansfeld, F.M.; Jackson, M.; Davis, T.P.; Kavallaris, M. Biologically Targeted Magnetic Hyperthermia: Potential and Limitations. *Front. Pharm.* **2018**, *9*. [CrossRef] [PubMed]
125. Chang, L.; Liu, X.L.; Di Fan, D.; Miao, Y.Q.; Zhang, H.; Ma, H.P.; Liu, Q.Y.; Ma, P.; Xue, W.M.; Luo, Y.E.; et al. The efficiency of magnetic hyperthermia and in vivo histocompatibility for human-like collagen protein-coated magnetic nanoparticles. *Int. J. Nanomed.* **2016**, *11*, 1175–1185.
126. Dutz, S.; Hergt, R.; Mürbe, J.; Töpfer, J.; Müller, R.; Zeisberger, M.; Andrä, W.; Bellemann, M.E. Magnetic Nanoparticles for Biomedical Heating Applications. *Z. Phys. Chem.* **2006**, *220*, 145–151. [CrossRef]
127. Long, N.V.; Yang, Y.; Teranishi, T.; Thi, C.; Cao, Y.; Nogami, M. Biomedical Applications of Advanced Multifunctional Magnetic Nanoparticles. *J. Nanosci. Nanotechnol.* **2015**, *15*, 10091–10107. [CrossRef]
128. Kim, D.; Shin, K.; Kwon, S.; Hyeon, T. Synthesis and Biomedical Applications of Multifunctional Nanoparticles. *Adv. Mater.* **2018**, *30*, 1802309. [CrossRef]
129. Abenojar, E.C.; Wickramasinghe, S.; Bas-Concepcion, J.; Samia, A.C.S. Structural effects on the magnetic hyperthermia properties of iron oxide nanoparticles. *Prog. Nat. Sci. Mater. Int.* **2016**, *26*, 440–448. [CrossRef]
130. Chung, C.; Kim, Y.-K.; Shin, D.; Ryoo, S.-R.; Hong, B.H.; Min, D.-H. Biomedical Applications of Graphene and Graphene Oxide. *Acc. Chem. Res.* **2013**, *46*, 2211–2224. [CrossRef]
131. Dembereldorj, U.; Kim, M.; Kim, S.; Ganbold, E.-O.; Lee, S.Y.; Joo, S.-W. A spatiotemporal anticancer drug release platform of PEGylated graphene oxide triggered by glutathione in vitro and in vivo. *J. Mater. Chem.* **2012**, *22*, 23845–23851. [CrossRef]
132. Liu, J.; Cui, L.; Losic, D. Graphene and graphene oxide as new nanocarriers for drug delivery applications. *Acta Biomater.* **2013**, *9*, 9243–9257. [CrossRef] [PubMed]
133. Liu, X.L.; Fan, H.M.; Yi, J.B.; Yang, Y.; Choo, E.S.G.; Xue, J.M.; Fan, D.D.; Ding, J. Optimization of surface coating on Fe3O4 nanoparticles for high performance magnetic hyperthermia agents. *J. Mater. Chem.* **2012**, *22*, 8235–8244. [CrossRef]
134. Venkatesha, N.; Qurishi, Y.; Atreya, H.S.; Srivastava, C. ZnO coated $CoFe_2O_4$ nanoparticles for multimodal bio-imaging. *RSC Adv.* **2016**, *6*, 18843–18851. [CrossRef]

135. Sundar, S.; Chen, Y.; Tong, Y.W. Delivery of therapeutics and molecules using self-assembled peptides. *Curr. Med. Chem.* **2014**, *21*, 2469–2479. [CrossRef]
136. Mazzotta, E.; Tavano, L.; Muzzalupo, R. Thermo-Sensitive Vesicles in Controlled Drug Delivery for Chemotherapy. *Pharmaceutics* **2018**, *10*, 150. [CrossRef]
137. Bi, H.; Xue, J.; Jiang, H.; Gao, S.; Yang, D.; Fang, Y.; Shi, K. Current developments in drug delivery with thermosensitive liposomes. *Asian J. Pharm. Sci.* **2019**, *14*, 365–379. [CrossRef]
138. Yadav, H.K.; Halabi, N.A.A.; Alsalloum, G.A. Nanogels as Novel Drug Delivery Systems—A Review. *J. Pharm. Pharm. Res.* **2017**, *1*, 1–8.
139. Blackburn, W.H.; Dickerson, E.B.; Smith, M.H.; McDonald, J.F.; Lyon, L.A. Peptide-Functionalized Nanogels for Targeted siRNA Delivery. *Bioconjug. Chem.* **2009**, *20*, 960–968. [CrossRef]
140. Cazares-Cortes, E.; Espinosa, A.; Guigner, J.-M.; Michel, A.; Griffete, N.; Wilhelm, C.; Ménager, C. Doxorubicin Intracellular Remote Release from Biocompatible Oligo(ethylene glycol) Methyl Ether Methacrylate-Based Magnetic Nanogels Triggered by Magnetic Hyperthermia. *ACS Appl. Mater. Interfaces* **2017**, *9*, 25775–25788. [CrossRef]
141. Cazares-Cortes, E.; Nerantzaki, M.; Fresnais, J.; Wilhelm, C.; Griffete, N.; Ménager, C. Magnetic Nanoparticles Create Hot Spots in Polymer Matrix for Controlled Drug Release. *Nanomaterials* **2018**, *8*, 850. [CrossRef] [PubMed]
142. Eslami, P.; Rossi, F.; Fedeli, S. Hybrid Nanogels: Stealth and Biocompatible Structures for Drug Delivery Applications. *Pharmaceutics* **2019**, *11*, 71. [CrossRef] [PubMed]
143. Oh, J.K.; Drumright, R.; Siegwart, D.J.; Matyjaszewski, K. The development of microgels/nanogels for drug delivery applications. *Prog. Polym. Sci.* **2008**, *33*, 448–477. [CrossRef]
144. Bharti, C.; Nagaich, U.; Pal, A.K.; Gulati, N. Mesoporous silica nanoparticles in target drug delivery system: A review. *Int. J. Pharm. Investig.* **2015**, *5*, 124–133. [CrossRef]
145. Wang, Y.; Zhao, Q.; Han, N.; Bai, L.; Li, J.; Liu, J.; Che, E.; Hu, L.; Zhang, Q.; Jiang, T.; et al. Mesoporous silica nanoparticles in drug delivery and biomedical applications. *Nanomedicine* **2015**, *11*, 313–327. [CrossRef]
146. Jafari, S.; Derakhshankhah, H.; Alaei, L.; Fattahi, A.; Varnamkhasti, B.S.; Saboury, A.A. Mesoporous silica nanoparticles for therapeutic/diagnostic applications. *Biomed. Pharmacother.* **2019**, *109*, 1100–1111. [CrossRef]
147. Mura, S.; Nicolas, J.; Couvreur, P. Stimuli-responsive nanocarriers for drug delivery. *Nat. Mater.* **2013**, *12*, 991–1003. [CrossRef]
148. Thomas, C.R.; Ferris, D.P.; Lee, J.-H.; Choi, E.; Cho, M.H.; Kim, E.S.; Stoddart, J.F.; Shin, J.-S.; Cheon, J.; Zink, J.I. Noninvasive Remote-Controlled Release of Drug Molecules in Vitro Using Magnetic Actuation of Mechanized Nanoparticles. *J. Am. Chem. Soc.* **2010**, *132*, 10623–10625. [CrossRef]
149. Coll, C.; Mondragón, L.; Martínez-Máñez, R.; Sancenón, F.; Marcos, M.D.; Soto, J.; Amorós, P.; Pérez-Payá, E. Enzyme-mediated controlled release systems by anchoring peptide sequences on mesoporous silica supports. *Angew. Chem. Int. Ed. Engl.* **2011**, *50*, 2138–2140. [CrossRef]
150. Lee, J.; Kim, H.; Kim, S.; Lee, H.; Kim, J.; Kim, N.; Park, H.J.; Choi, E.K.; Lee, J.S.; Kim, C. A multifunctional mesoporous nanocontainer with an iron oxide core and a cyclodextrin gatekeeper for an efficient theranostic platform. *J. Mater. Chem.* **2012**, *22*, 14061–14067. [CrossRef]
151. Guisasola, E.; Asín, L.; Beola, L.; de la Fuente, J.M.; Baeza, A.; Vallet-Regí, M. Beyond Traditional Hyperthermia: In Vivo Cancer Treatment with Magnetic-Responsive Mesoporous Silica Nanocarriers. *ACS Appl. Mater. Interfaces* **2018**, *10*, 12518–12525. [CrossRef] [PubMed]
152. Gandhi, A.; Paul, A.; Sen, S.O.; Sen, K.K. Studies on thermoresponsive polymers: Phase behaviour, drug delivery and biomedical applications. *Asian J. Pharm. Sci.* **2015**, *10*, 99–107. [CrossRef]
153. Cheng, L.; Yang, K.; Li, Y.; Zeng, X.; Shao, M.; Lee, S.-T.; Liu, Z. Multifunctional nanoparticles for upconversion luminescence/MR multimodal imaging and magnetically targeted photothermal therapy. *Biomaterials* **2012**, *33*, 2215–2222. [CrossRef] [PubMed]
154. Park, H.; Yang, J.; Seo, S.; Kim, K.; Suh, J.; Kim, D.; Haam, S.; Yoo, K.-H. Multifunctional nanoparticles for photothermally controlled drug delivery and magnetic resonance imaging enhancement. *Small* **2008**, *4*, 192–196. [CrossRef] [PubMed]
155. Ma, X.; Tao, H.; Yang, K.; Feng, L.; Cheng, L.; Shi, X.; Li, Y.; Guo, L.; Liu, Z. A functionalized graphene oxide-iron oxide nanocomposite for magnetically targeted drug delivery, photothermal therapy, and magnetic resonance imaging. *Nano Res.* **2012**, *5*, 199–212. [CrossRef]

156. Yao, X.; Niu, X.; Ma, K.; Huang, P.; Grothe, J.; Kaskel, S.; Zhu, Y. Graphene Quantum Dots-Capped Magnetic Mesoporous Silica Nanoparticles as a Multifunctional Platform for Controlled Drug Delivery, Magnetic Hyperthermia, and Photothermal Therapy. *Small* **2017**, *13*, 1602225. [CrossRef]
157. Ma, Y.; Liang, X.; Tong, S.; Bao, G.; Ren, Q.; Dai, Z. Gold Nanoshell Nanomicelles for Potential Magnetic Resonance Imaging, Light-Triggered Drug Release, and Photothermal Therapy. *Adv. Funct. Mater.* **2013**, *23*, 815–822. [CrossRef]
158. Fu, S.; Ding, Y.; Cong, T.; Yang, X.; Hong, X.; Yu, B.; Li, Y.; Liu, Y. Multifunctional $NaYF_4$:Yb,Er@PE_3@Fe_3O_4 nanocomposites for magnetic-field-assisted upconversion imaging guided photothermal therapy of cancer cells. *Dalton Trans.* **2019**, *48*, 12850–12857. [CrossRef]
159. Buzug, T.M.; Bringout, G.; Erbe, M.; Gräfe, K.; Graeser, M.; Grüttner, M.; Halkola, A.; Sattel, T.F.; Tenner, W.; Wojtczyk, H.; et al. Magnetic particle imaging: Introduction to imaging and hardware realization. *Z Med. Phys.* **2012**, *22*, 323–334. [CrossRef]
160. Lim, J.-W.; Son, S.U.; Lim, E.-K. *Recent Advances in Bioimaging for Cancer Research. State of the Art Nano-Bioimaging*; Ghamsari, M.S., Ed.; IntechOpen: London, UK, 2018; pp. 11–33.
161. Wu, L.C.; Zhang, Y.; Steinberg, G.; Qu, H.; Huang, S.; Cheng, M.; Bliss, T.; Du, F.; Rao, J.; Song, G.; et al. A Review of Magnetic Particle Imaging and Perspectives on Neuroimaging. *Am. J. Neuroradiol.* **2019**, *40*, 206–212. [CrossRef]
162. Reddy, L.H.; Arias, J.L.; Nicolas, J.; Couvreur, P. Magnetic Nanoparticles: Design and Characterization, Toxicity and Biocompatibility, Pharmaceutical and Biomedical Applications. *Chem. Rev.* **2012**, *112*, 5818–5878. [CrossRef] [PubMed]
163. Tay, Z.W.; Chandrasekharan, P.; Chiu-Lam, A.; Hensley, D.W.; Dhavalikar, R.; Zhou, X.Y.; Yu, E.Y.; Goodwill, P.W.; Zheng, B.; Rinaldi, C.; et al. Magnetic Particle Imaging-Guided Heating in Vivo Using Gradient Fields for Arbitrary Localization of Magnetic Hyperthermia Therapy. *ACS Nano* **2018**, *12*, 3699–3713. [CrossRef] [PubMed]
164. Basly, B.; Popa, G.; Fleutot, S.; Pichon, B.P.; Garofalo, A.; Ghobril, C.; Billotey, C.; Berniard, A.; Bonazza, P.; Martinez, H.; et al. Effect of the nanoparticle synthesis method on dendronized iron oxides as MRI contrast agents. *Dalton Trans.* **2013**, *42*, 2146–2157. [CrossRef] [PubMed]
165. Sun, J.; Zhou, S.; Hou, P.; Yang, Y.; Weng, J.; Li, X.; Li, M. Synthesis and characterization of biocompatible Fe_3O_4 nanoparticles. *J. Biomed. Mater. Res. A* **2007**, *80*, 333–341. [CrossRef]
166. Liu, Z.; Zhang, D.; Han, S.; Li, C.; Lei, B.; Lu, W.; Fang, J.; Zhou, C. Single Crystalline Magnetite Nanotubes. *J. Am. Chem. Soc.* **2005**, *127*, 6–7. [CrossRef]
167. Zhong, Z.; Lin, M.; Ng, V.; Ng, G.X.B.; Foo, Y.; Gedanken, A. A Versatile Wet-Chemical Method for Synthesis of One-Dimensional Ferric and Other Transition Metal Oxides. *Chem. Mater.* **2006**, *18*, 6031–6036. [CrossRef]
168. Jiao, F.; Jumas, J.-C.; Womes, M.; Chadwick, A.V.; Harrison, A.; Bruce, P.G. Synthesis of Ordered Mesoporous Fe_3O_4 and γ-Fe_2O_3 with Crystalline Walls Using Post-Template Reduction/Oxidation. *J. Am. Chem. Soc.* **2006**, *128*, 12905–12909. [CrossRef]
169. Du, N.; Xu, Y.; Zhang, H.; Zhai, C.; Yang, D. Selective Synthesis of Fe_2O_3 and Fe_3O_4 Nanowires Via a Single Precursor: A General Method for Metal Oxide Nanowires. *Nanoscale Res. Lett.* **2010**, *5*, 1295–1300. [CrossRef]
170. Wang, G.; Wang, C.; Dou, W.; Ma, Q.; Yuan, P.; Su, X. The synthesis of magnetic and fluorescent bi-functional silica composite nanoparticles via reverse microemulsion method. *J. Fluoresc.* **2009**, *19*, 939–946. [CrossRef]
171. Jin, J.; Ohkoshi, S.; Hashimoto, K. Giant Coercive Field of Nanometer- Sized Iron Oxide. *Adv. Mater.* **2004**, *16*, 48–51. [CrossRef]
172. Han, Y.C.; Cha, H.G.; Kim, C.W.; Kim, Y.H.; Kang, Y.S. Synthesis of Highly Magnetized Iron Nanoparticles by a Solventless Thermal Decomposition Method. *J. Phys. Chem. C* **2007**, *111*, 6275–6280. [CrossRef]
173. Sun, S.; Zeng, H. Size-controlled synthesis of magnetite nanoparticles. *J. Am. Chem. Soc.* **2002**, *124*, 8204–8205. [CrossRef] [PubMed]
174. Ai, L.; Zhang, C.; Chen, Z. Removal of methylene blue from aqueous solution by a solvothermal-synthesized graphene/magnetite composite. *J. Hazard. Mater.* **2011**, *192*, 1515–1524. [CrossRef] [PubMed]
175. Kang, M. Synthesis of Fe/TiO_2 photocatalyst with nanometer size by solvothermal method and the effect of H2O addition on structural stability and photodecomposition of methanol. *J. Mol. Catal. A Chem.* **2003**, *197*, 173–183. [CrossRef]
176. Park, J.; An, K.; Hwang, Y.; Park, J.-G.; Noh, H.-J.; Kim, J.-Y.; Park, J.-H.; Hwang, N.-M.; Hyeon, T. Ultra-large-scale syntheses of monodisperse nanocrystals. *Nat. Mater.* **2004**, *3*, 891–895. [CrossRef]

177. Teja, A.; Koh, P.Y. Synthesis, properties, and applications of magnetic iron oxide nanoparticles. *Prog. Cryst. Growth Charact. Mater.* **2009**, *55*, 22–45. [CrossRef]
178. Guo, Q.; Teng, X.; Rahman, S.; Yang, H. Patterned Langmuir−Blodgett Films of Monodisperse Nanoparticles of Iron Oxide Using Soft Lithography. *J. Am. Chem. Soc.* **2003**, *125*, 630–631. [CrossRef]
179. Taniguchi, I. Powder properties of partially substituted LiMxMn2−xO4 (M=Al, Cr, Fe and Co) synthesized by ultrasonic spray pyrolysis. *Mater. Chem. Phys.* **2005**, *92*, 172–179. [CrossRef]
180. Dosev, D.; Nichkova, M.; Dumas, R.K.; Gee, S.J.; Hammock, B.D.; Liu, K.; Kennedy, I.M. Magnetic/luminescent core/shell particles synthesized by spray pyrolysis and their application in immunoassays with internal standard. *Nanotechnology* **2007**, *18*, 055102. [CrossRef]
181. Polshettiwar, V.; Baruwati, B.; Varma, R.S. Self-Assembly of Metal Oxides into Three-Dimensional Nanostructures: Synthesis and Application in Catalysis. *ACS Nano* **2009**, *3*, 728–736. [CrossRef]
182. Jia, C.-J.; Sun, L.-D.; Luo, F.; Han, X.-D.; Heyderman, L.J.; Yan, Z.-G.; Yan, C.-H.; Zheng, K.; Zhang, Z.; Takano, M.; et al. Large-Scale Synthesis of Single-Crystalline Iron Oxide Magnetic Nanorings. *J. Am. Chem. Soc.* **2008**, *130*, 16968–16977. [CrossRef] [PubMed]
183. Li, Z.; Wei, L.; Gao, M.Y.; Lei, H. One-Pot Reaction to Synthesize Biocompatible Magnetite Nanoparticles. *Adv. Mater.* **2005**, *17*, 1001–1005. [CrossRef]
184. Jana, N.R.; Chen, Y.; Peng, X. Size- and Shape-Controlled Magnetic (Cr, Mn, Fe, Co, Ni) Oxide Nanocrystals via a Simple and General Approach. *Chem. Mater.* **2004**, *16*, 3931–3935. [CrossRef]
185. Rockenberger, J.; Scher, E.C.; Alivisatos, A.P. A New Nonhydrolytic Single-Precursor Approach to Surfactant-Capped Nanocrystals of Transition Metal Oxides. *J. Am. Chem. Soc.* **1999**, *121*, 11595–11596. [CrossRef]
186. Zeng, H.; Li, J.; Liu, J.P.; Wang, Z.L.; Sun, S. Exchange-coupled nanocomposite magnets by nanoparticle self-assembly. *Nature* **2002**, *420*, 395–398. [CrossRef]
187. Salazar-Alvarez, G.; Qin, J.; Šepelák, V.; Bergmann, I.; Vasilakaki, M.; Trohidou, K.N.; Ardisson, J.D.; Macedo, W.A.A.; Mikhaylova, M.; Muhammed, M.; et al. Cubic versus Spherical Magnetic Nanoparticles: The Role of Surface Anisotropy. *J. Am. Chem. Soc.* **2008**, *130*, 13234–13239. [CrossRef]
188. Hayashi, H.; Hakuta, Y. Hydrothermal Synthesis of Metal Oxide Nanoparticles in Supercritical Water. *Materials* **2010**, *3*, 3794–3817. [CrossRef]
189. Yu, J.; Yu, X. Hydrothermal Synthesis and Photocatalytic Activity of Zinc Oxide Hollow Spheres. *Environ. Sci. Technol.* **2008**, *42*, 4902–4907. [CrossRef]
190. Yang, T.; Li, Y.; Zhu, M.; Huang, J.; Jin, H.; Hu, Y. Room-temperature ferromagnetic Mn-doped ZnO nanocrystal synthesized by hydrothermal method under high magnetic field. *Mater. Sci. Eng. B-Adv. Funct. Solid-State Mater.* **2010**, *170*, 129–132. [CrossRef]
191. Hu, J.; Bando, Y. Growth and Optical Properties of Single-Crystal Tubular ZnO Whiskers. *Appl. Phys. Lett.* **2003**, *82*, 1401–1403. [CrossRef]
192. Wang, X.; Zhuang, J.; Peng, Q.; Li, Y. A general strategy for nanocrystal synthesis. *Nature* **2005**, *437*, 121–124. [CrossRef] [PubMed]
193. Sun, S.; Zeng, H.; Robinson, D.B.; Raoux, S.; Rice, P.M.; Wang, S.X.; Li, G. Monodisperse MFe2O4 (M = Fe, Co, Mn) Nanoparticles. *J. Am. Chem. Soc.* **2004**, *126*, 273–279. [CrossRef] [PubMed]
194. Wu, W.; Hao, R.; Liu, F.; Su, X.; Hou, Y. Single-crystalline α-Fe_2O_3 nanostructures: Controlled synthesis and high-index plane-enhanced photodegradation by visible light. *J. Mater. Chem. A* **2013**, *1*, 6888–6894. [CrossRef]
195. Zeng, Y.; Hao, R.; Xing, B.; Hou, Y.; Xu, Z. One-pot synthesis of Fe_3O_4 nanoprisms with controlled electrochemical properties. *Chem. Commun.* **2010**, *46*, 3920–3922. [CrossRef] [PubMed]
196. Weiwei, W. Microwave-induced polyol-process synthesis of $M^{II}Fe_2O_4$ (M = Mn, Co) nanoparticles and magnetic property. *Mater. Chem. Phys.* **2008**, *108*, 227–231.
197. Wang, W.-W.; Zhu, Y.-J.; Ruan, M.-L. Microwave-assisted synthesis and magnetic property of magnetite and hematite nanoparticles. *J. Nanopart. Res.* **2007**, *9*, 419–426. [CrossRef]
198. Sander, D.; Oka, H.; Corbetta, M.; Stepanyuk, V.; Kirschner, J. New insights into nano-magnetism by spin-polarized scanning tunneling microscopy. *J. Electron. Spectrosc. Relat. Phenom.* **2013**, *189*, 206–215. [CrossRef]
199. Hurst, S.J.; Payne, E.K.; Qin, L.; Mirkin, C.A. Multisegmented one-dimensional nanorods prepared by hard-template synthetic methods. *Angew. Chem. Int. Ed. Engl.* **2006**, *45*, 2672–2692. [CrossRef]

200. Lam, T.; Pouliot, P.; Avti, P.K.; Lesage, F.; Kakkar, A.K. Superparamagnetic iron oxide based nanoprobes for imaging and theranostics. *Adv. Colloid Interface Sci.* **2013**, *199–200*, 95–113. [CrossRef]
201. Cui, H.; Liu, Y.; Ren, W. Structure switch between alpha-Fe_2O_3, gamma-Fe_2O_3 and Fe_3O_4 during the large scale and low temperature sol-gel synthesis of nearly monodispersed iron oxide nanoparticles. *Adv. Powder Technol.* **2013**, *24*, 93–97. [CrossRef]
202. Xu, J.; Yang, H.; Fu, W.; Du, K.; Sui, Y.; Chen, J.; Yi, Z.; Li, M.; Zou, G. Preparation and Magnetic Properties of Magnetite Nanoparticles by Sol–Gel Method. *J. Magn. Magn. Mater.* **2010**, *309*, 307–311. [CrossRef]
203. Bilecka, I.; Elser, P.; Niederberger, M. Kinetic and Thermodynamic Aspects in the Microwave-Assisted Synthesis of ZnO Nanoparticles in Benzyl Alcohol. *ACS Nano* **2009**, *3*, 467–477. [CrossRef] [PubMed]
204. Bilecka, I.; Kubli, M.; Amstad, E.; Niederberger, M. Simultaneous formation of ferrite nanocrystals and deposition of thin films via a microwave-assisted nonaqueous sol–gel process. *J. Sol. Gel Sci. Technol.* **2011**, *57*, 313–322. [CrossRef]
205. Marcano, D.C.; Kosynkin, D.V.; Berlin, J.M.; Sinitskii, A.; Sun, Z.; Slesarev, A.; Alemany, L.B.; Lu, W.; Tour, J.M. Improved Synthesis of Graphene Oxide. *ACS Nano* **2010**, *4*, 4806–4814. [CrossRef]
206. Venkatesha, N.; Poojar, P.; Qurishi, Y.; Geethanath, S.; Srivastava, C. Graphene oxide-Fe_3O_4 nanoparticle composite with high transverse proton relaxivity value for magnetic resonance imaging. *J. Appl. Phys.* **2015**, *117*, 154702. [CrossRef]
207. Kumar, V.; Sharma, N.; Maitra, S.S. In vitro and in vivo toxicity assessment of nanoparticles. *Int. Nano Lett.* **2017**, *7*, 243–256. [CrossRef]
208. Khalili Fard, J.; Jafari, S.; Eghbal, M.A. A Review of Molecular Mechanisms Involved in Toxicity of Nanoparticles. *Adv. Pharm. Bull.* **2015**, *5*, 447–454. [CrossRef]
209. Demirer, G.S.; Okur, A.C.; Kizilel, S. Synthesis and design of biologically inspired biocompatible iron oxide nanoparticles for biomedical applications. *J. Mater. Chem. B* **2015**, *3*, 7831–7849. [CrossRef]
210. Zahraei, M.; Marciello, M.; Lazaro-Carrillo, A.; Villanueva, A.; Herranz, F.; Talelli, M.; Costo, R.; Monshi, A.; Shahbazi-Gahrouei, D.; Amirnasr, M.; et al. Versatile theranostics agents designed by coating ferrite nanoparticles with biocompatible polymers. *Nanotechnology* **2016**, *27*, 255702. [CrossRef]
211. Aslantürk, Ö.S. In Vitro Cytotoxicity and Cell Viability Assays: Principles, Advantages, and Disadvantages. In *Genotoxicity A Predictable Risk to Our Actual World*; Larramendy, M., Ed.; IntechOpen: London, UK, 2018; pp. 1–17.
212. Pasukonienė, V.; Mlynska, A.; Steponkienė, S.; Poderys, V.; Matulionytė, M.; Karabanovas, V.; Statkutė, U.; Purvinienė, R.; Kraśko, J.A.; Jagminas, A.; et al. Accumulation and biological effects of cobalt ferrite nanoparticles in human pancreatic and ovarian cancer cells. *Medicina* **2014**, *50*, 237–244. [CrossRef]